AGU PUBLICATIONS

JGR

Journal of Geophysical Research: Space Physics

RESEARCH ARTICLE
10.1002/2014JA020412

Key Points:
- A categorization based on entropy, Alfven speed, and temperature is developed
- Tests show the three-parameter scheme is an improvement over existing schemes
- The scheme categorizes a fourth type of plasma: sector-reversal-region plasma

Correspondence to:
J. E. Borovsky,
jborovsky@spacescience.org

Citation:
Xu, F., and J. E. Borovsky (2015), A new four-plasma categorization scheme for the solar wind, *J. Geophys. Res. Space Physics*, *120*, 70–100, doi:10.1002/2014JA020412.

Received 21 JUL 2014
Accepted 12 DEC 2014
Accepted article online 15 DEC 2014
Published online 29 JAN 2015

A new four-plasma categorization scheme for the solar wind

Fei Xu[1,2] and Joseph E. Borovsky[3,4,5]

[1]Physics Department, Nanjing University of Information Science and Technology, Nanjing, China, [2]CSPAR, University of Alabama, Huntsville, Alabama, USA, [3]Center for Space Plasma Physics, Space Science Institute, Boulder, Colorado, USA, [4]AOSS, University of Michigan, Ann Arbor, Michigan, USA, [5]Physics Department, Lancaster University, Lancaster, UK

Abstract A three-parameter algebraic scheme is developed to categorize the solar wind at 1 AU into four plasma types: coronal-hole-origin plasma, streamer-belt-origin plasma, sector-reversal-region plasma, and ejecta. The three parameters are the proton-specific entropy $S_p = T_p/n_p^{2/3}$, the proton Alfvén speed v_A, and the proton temperature T_p compared with a velocity-dependent expected temperature. Four measurements are needed to apply the scheme: the proton number density n_p, the proton temperature T_p, the magnetic field strength B, and the solar wind speed v_{sw}. The scheme is tested and is found to be more accurate than existing categorization schemes. The categorization scheme is applied to the 1963–2013 OMNI2 data set spanning four solar cycles and to the 1998–2008 ACE data set. The statistical properties of the four types of plasma are examined. The sector-reversal-region plasma is found to have statistically low alpha-to-proton density ratios and high Alfvén Mach numbers. The statistical relations between the proton and alpha-particle-specific entropies and oxygen and carbon charge-state-density ratios S_p, S_α, O^{7+}/O^{6+}, and C^{6+}/C^{5+} from ACE are examined for the four types of plasma: the patterns observed imply a connection between sector-reversal-region plasma and ejecta and a connection between streamer-belt-origin plasma and coronal-hole-origin plasma. Plasma occurrence rates are examined and solar cycle patterns are found for ejecta, for coronal-hole-origin plasma, and for sector-reversal-region plasma.

1. Introduction

A four-plasma categorization scheme at 1 AU will be developed based on measurements of the solar wind proton density and temperature, the solar wind speed, and the solar wind magnetic field strength. An advantage of the new categorization scheme is that it does not rely upon heavy ion measurements.

1.1. The Plasma Types in the Solar Wind

It is generally accepted that there are three major types of solar wind plasma, coronal-hole-origin plasma, streamer-belt-origin plasma, and ejecta. Ejecta are associated with solar transients such as coronal mass ejections [cf. *Richardson et al.*, 2000; *Zhao et al.*, 2009]. In this report streamer belt plasma will be divided further into two subgroups [cf. *Antonucci et al.*, 2005; *Schwenn*, 2006; *Susino et al.*, 2008]: (a) streamer belt plasma and (b) sector reversal regions.

Coronal-hole-origin plasma is sometimes referred to as the fast solar wind; it originates from the interaction of open field lines with the low-lying closed loops on the floor of a coronal hole [*Sheeley et al.*, 1976; *Cranmer*, 2009] (see Figure 1). Streamer-belt-origin plasma is sometimes referred to as the slow solar wind. Where it originates is of some controversy (see Figure 1); streamer belt plasma is believed to come from either (a) the interchange reconnection of open magnetic field lines with closed streamer belt field lines [*Fisk et al.*, 1999; *Subramanian et al.*, 2010; *Antiochos et al.*, 2011; *Crooker et al.*, 2012] or (b) the edge of a coronal hole near a streamer belt [*Wang and Sheeley*, 1990; *Arge et al.*, 2003]. The sector-reversal-region plasma is likely emitted from the top of the helmet streamers [*Gosling et al.*, 1981; *Susino et al.*, 2008; *Suess et al.*, 2009; *Foullon et al.*, 2011] (see Figure 1).

There are statistical differences between coronal-hole-origin plasma and streamer-belt-origin plasma. Coronal-hole-origin plasma tends to be homogeneous whereas streamer-belt-origin plasma is highly structured [*Bame et al.*, 1977; *Borovsky*, 2012c]; coronal-hole-origin plasma is dominated by outward Alfvénic fluctuations whereas streamer-belt-origin plasma is not very Alfvénic [*Luttrell and Richter*, 1988; *Schwenn*, 1990; *Borovsky and Denton*, 2010a]. Coronal hole plasma is characterized by an alpha-proton

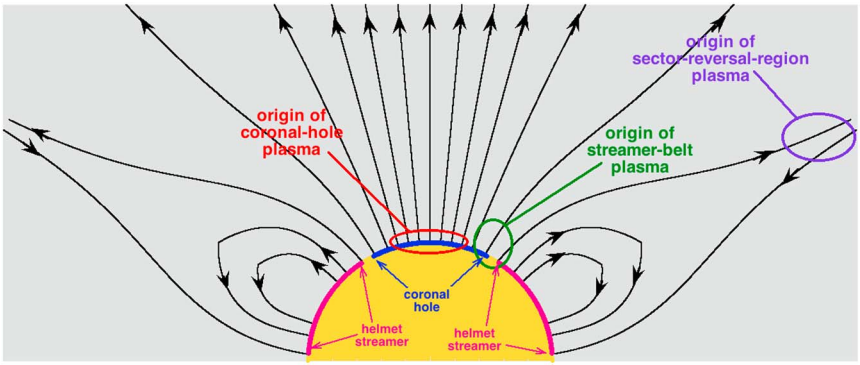

Figure 1. A sketch of the Sun (yellow) with a coronal hole surrounded by two helmet streamers (pink labels). The source locations of three types of plasma are indicated with the circles: coronal-hole-origin plasma (red), sector-reversal-region plasma (purple), and streamer-belt-origin plasma (green). The streamer belt plasma may come from the edge of the coronal hole near the streamer belt and/or interchange reconnection between open flux and the closed loops of the streamer belt.

field-aligned relative drift at up to the local proton Alfvén speed [*Marsch et al.*, 1982], with such alpha-proton relative streaming typically absent in streamer-belt-origin plasma [*Hirshberg et al.*, 1974; *Asbridge et al.*, 1976]. Coronal hole plasma exhibits a statistical nonadiabatic heating of the protons with distance from the Sun in the inner heliosphere [*Hellinger et al.*, 2011; *Borovsky and Gary*, 2014]; the protons of streamer-belt-origin plasma are closer to adiabatic [*Eyni and Steinitz*, 1978; *Freeman and Lopez*, 1985]. The Fourier spectral indices of the magnetic field fluctuations, the velocity fluctuations, and the Elsasser variables show statistical differences between the two types of plasma [*Tu and Marsch*, 1995; *Borovsky*, 2012a]. Current sheets in coronal hole plasma are colocated with velocity shears [*Borovsky*, 2012b]; current sheets in streamer belt plasma are colocated with plasma boundaries [*Borovsky*, 2012c]. Almost any study done of the solar wind needs to be organized by the origin of the solar wind plasma.

Intervals of streamer belt plasma in the data time series can be categorized as either helmet streamers or pseudostreamers. Helmet streamers form at the Sun when a loop arcade separates two coronal holes of opposite magnetic polarity [*Pneuman*, 1968; *Rusin et al.*, 2010]. Pseudostreamers form when two like-signed coronal holes are separated by a pair of loop arcades [*Wang et al.*, 2007; *Riley and Luhmann*, 2012]. A helmet streamer interval is identified at 1 AU as an interval of streamer belt plasma separating two coronal-hole-plasma regions with opposite magnetic polarity; a pseudostreamer interval is identified at 1 AU as an interval of streamer belt plasma separating two coronal hole regions with the same magnetic polarity [*Borovsky and Denton*, 2013]. Within a helmet streamer interval there is one sector reversal (which can be multiply structured [*Crooker et al.*, 1993, 2004a; *Blanco et al.*, 2006; *Foullon et al.*, 2009]). Within a pseudostreamer interval there is thought to be zero sector reversals, but one cannot rule out pseudostreamer intervals with an even number of sector reversals [cf. *Wang et al.*, 2007; *Panasenco and Velli*, 2013].

As will be seen, around the sector reversal of a helmet streamer there is an interval of plasma that has very low proton-specific entropy, high-number densities, either an absence of an electron strahl or a very intermittent electron strahl, a low alpha-to-proton density ratio, and typically a very low velocity. These intervals of distinct plasma will be cataloged as "sector reversal regions." Pseudostreamer intervals without sector reversals do not have this sector-reversal-region type of plasma in them [see also *Neugebauer et al.*, 2004; *Wang et al.*, 2012].

The other major category of solar wind plasma is termed "ejecta," also denoted as "interplanetary coronal mass ejections" (ICMEs). Ejecta include magnetic clouds, which are structures that have an enhanced, rotating magnetic field, low proton temperature, and low beta. The ejecta originate as streamer belt or active region magnetic structures that became disconnected. Unlike plasmas that are steadily emitted from the Sun, the magnetic fields in impulsively emitted ejecta do not follow the Parker spiral [*Borovsky*, 2010]. Whereas steadily emitted solar wind expands in the two directions transverse to radial as it advects from the Sun, impulsive ejecta can expand in all three directions as they propagate outward [*Klein and Burlaga*, 1982; *Poomvises et al.*, 2010]. This overexpansion results (usually) in anomalously low plasma temperatures at 1 AU

for ejecta [*Gosling et al*., 1973; *Elliott et al*., 2005]. The closed loop structures can often be detected by bidirectional electron strahls (indicating both magnetic foot points on the Sun) [*Gosling et al*., 1987; *Richardson and Cane*, 2010]. There are a number of additional signatures of ejecta [cf. *Neugebauer and Goldstein*, 1997; *Lepping et al*., 2005; *Zurbuchen and Richardson*, 2006].

1.2. Why Categorization of the Solar Wind Is Important

A categorization of the solar wind into its four types of plasma is desirable for a number of reasons. From the above discussion, it is clear that the properties of the four types of solar wind differ considerably. Hence, when, for example, making a statistical study of solar wind parameters, the interpretation of the results can be clarified by dividing the solar wind measurements according to the type of solar wind in which they were observed.

Through the different phases of the solar cycle the occurrence rates at Earth of the various types of solar wind plasma systematically change [*Intriligator*, 1974; *Bame et al*., 1976; *Zhao et al*., 2009; *D'Amicis et al*., 2011; *Richardson and Cane*, 2012; *Lepri et al*., 2013]. Recent studies have reported a solar cycle variation in the manner by which the solar wind drives the Earth [*Nakai and Kamide*, 1999; *Nagatsuma*, 2006; *McPherron et al*., 2009, 2013; *Burke*, 2011]. The solar cycle variation in the driving of the Earth should really be caused by differences in the solar wind driving with plasma type. This root cause has never been investigated.

Finally, to use solar wind measurements at 1 AU to diagnose physical processes ongoing at the Sun and to infer the properties of the solar wind at the Sun [*Mariani et al*., 1983; *Thieme et al*., 1988, 1989, 1990; *Matthaeus et al*., 2007; *Borovsky*, 2008; *Zastenker et al*., 2014], those solar wind measurements must be sorted according to their origin.

1.3. Existing Solar Wind Categorization Methodologies

If the solar wind plasma is categorized, it is usually simply separated into "fast wind" or "slow wind" according to the speed of the wind [e.g., *Arya and Freeman*, 1991; *Tu and Marsch*, 1995; *Feldman et al*., 2005; *Yordanova et al*., 2009; *Bruno and Carbone*, 2013]. This roughly separates the plasma into coronal hole versus streamer belt origin (see section 3.1), except (a) when there are compressions or rarefactions, (b) when coronal holes are small and the solar wind speed at Earth is not fast, or (c) when ejecta are present. This velocity scheme also does not separate out sector-reversal-region plasma.

Many methodologies have been developed to identify and separate ejecta (ICMEs and magnetic clouds). These may focus on anomalously low proton temperatures [*Gosling et al*., 1973; *Richardson and Cane*, 1995; *Elliott et al*., 2005], on low levels of magnetic field fluctuations [*Lepping et al*., 2005], or on the presence of a bidirectional electron strahl [*Gosling et al*., 1987; *Skoug et al*., 2000]. *Richardson and Cane* [2010] [see also *Cane and Richardson*, 2003] produced an extensive list of ejecta intervals at Earth based on the combination of proton temperature, O^{7+}/O^{6+} density ratio, electron strahl, magnetic field structure, and energetic particle measurements. A catalog of magnetic clouds at Earth [e.g., *Lepping et al*., 2005] based on plasma beta and magnetic field structure has been produced and a catalog of ICMEs at Earth [*Jian et al*., 2006] based on the total pressure, the proton temperature, the alpha-to-proton density ratio, the magnetic field structure, and the presence of bidirectional electron streaming has been produced.

Zhao et al. [2009] [see also *Zurbuchen et al*., 2002; *von Steiger et al*., 2010] constructed an algorithm to categorize the 1998–2008 ACE solar wind data set into coronal-hole-origin plasma, noncoronal-hole-origin plasma (streamer belt origin), and ejecta based on the O^{7+}/O^{6+} density ratio and the wind speed. In Figure 2 the Zhao et al. O^{7+}/O^{6+} versus v_{sw} scheme is applied to four collections of plasma in the solar wind: a collection of unperturbed coronal hole wind (red), a collection of pseudostreamer wind [*Borovsky and Denton*, 2013] (green), a collection of regions around sector reversals where the electron strahl becomes intermittent (purple), and the collection of Lepping magnetic clouds [*Lepping et al*., 2005] http://wind.gsfc.nasa.gov/mfi/mag_cloud_pub1.html (blue). (These collections are described further in section 2.1.) As can be seen, the Zhao et al. O^{7+}/O^{6+} versus v_{sw} categorization scheme does a good job of separating the distinct types of solar wind in the four collections of events. Note that a drawback to using the Zhao et al. scheme is that O^{7+}/O^{6+} measurements are not generally available in solar wind data sets, i.e., most solar wind spacecraft do not carry ion composition instrumentation.

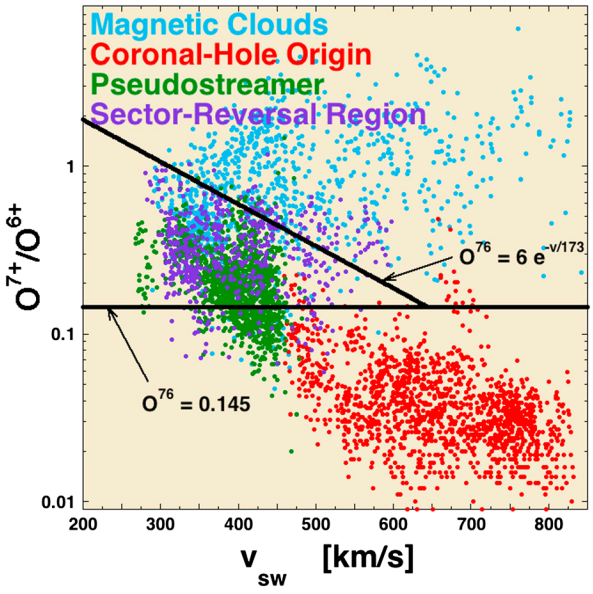

Figure 2. Hourly averaged values of solar wind data are plotted for four collections of wind types: unperturbed coronal-hole-origin wind (red), pseudostreamers (streamer-belt-origin wind, green), sector reversal regions (purple), and the Lepping magnetic clouds (blue). The four known types of wind are plotted in the *Zhao et al.* [2009] O^{7+}/O^{6+} versus v_{sw} scheme (black curves). In the *Zhao et al.* [2009] scheme the top domain is ejecta, the lower domain is coronal-hole-origin plasma, and the middle domain is non-coronal-hole-origin plasma.

Another plasma categorization scheme recently used [*Borovsky and Denton*, 2014] focuses on the parameter P_{type} (plasma type)

$$P_{type} = \log(S_p) + \log(S_\alpha) - \log(O^{7+}/O^{6+}) - \log(C^{6+}/C^{5+}) \quad (1)$$

where $S_p = T_p/n_p^{2/3}$ is the proton-specific entropy of the solar wind, $S_\alpha = T_\alpha/n_\alpha^{2/3}$ is the alpha-particle-specific entropy of the solar wind, and where O^{7+}/O^{6+} and C^{6+}/C^{5+} are the oxygen and carbon charge-state number density ratios in the solar wind.

The *Genesis* spacecraft had an onboard solar wind classification algorithm [*Neugebauer et al.*, 2003; *Reisenfeld et al.*, 2003] that used measurements of the alpha-to-proton density ratio, the strength of bidirectional electron strahl, the proton temperature, and the solar wind speed. The algorithm used not only the measurements but also the time history of measurements and the time history of the occurrence of interplanetary shocks.

1.4. The Present Work

This manuscript is organized as follows. In section 2 the development of the three-parameter four-plasma categorization scheme for the solar wind is described. In section 3 the categorization scheme is applied to the1963–2013 OMNI2 data set and the properties of the four types of plasmas are investigated. Using the categorized 1963–2013 OMNI2 data set, the occurrence rates of the four types of solar wind plasma are examined over four solar cycles in section 4. Section 5 contains a summary of the findings, and section 6 contains discussions about the sector reversal region plasma and about future research.

2. Developing the Three-Paramater Categorization Scheme

A three-parameter four-plasma-type categorization scheme for the solar wind at 1 AU will be developed by (1) making collections of solar wind data of known plasma types and (2) using those collections to develop algebraic rules to describe the domains of the four plasmas in parameter space.

The data sets used in this development, testing, and statistical investigation are the 1963–2013 OMNI2 data [*King and Papitashvili*, 2005] set of 1 h averaged solar wind parameters, the 1998–2013 ACE SWEPAM (Solar Wind Electron, Proton, and Alpha Monitor) [*McComas et al.*, 1998] proton and electron data sets, the 1998–2011 ACE SWICS (Solar Wind Ion Composition Spectrometer) [*Gloeckler et al.*, 1998] solar wind ion data sets, and the 1998–2013 ACE Mag [*Smith et al.*, 1998] magnetic field data set. From ACE SWICS, 1 h averaged quantities are used, and only values that are flagged as "good quality" in the data set are employed.

2.1. Collecting the Ideal Events

For use in developing and testing solar wind categorization schemes, large collections of plasma of known types are needed. The collection used here are (a) unperturbed coronal-hole-origin solar wind, (b) pseudostreamer solar wind, (c) the regions around sector reversals, and (d) magnetic clouds.

For the unperturbed coronal-hole-origin solar wind, intervals of steady-velocity high-speed streams were collected. From the ACE SWEPAM, SWICS, and Mag instruments, temporal plots of v_{sw}, S_p, O^{7+}/O^{6+}, C^{6+}/C^{5+}, and the latitude and longitude of the interplanetary magnetic field (IMF) from ACE were examined.

Twenty-seven day repeating high-speed streams are easily found, and only streams with long (days) intervals of steady speed wind were used. The unperturbed coronal hole intervals selected did not commence until the solar wind reached a steady speed (after the compression of the corotating interaction region), and the intervals ended before the solar wind speed begins to drop at the onset of the tailing edge rarefaction. To ensure that the high-speed stream intervals were not contaminated with ejecta, S_p, O^{7+}/O^{6+}, and C^{6+}/C^{5+} were monitored to exclude high-speed streams wherein large jumps in S_p, O^{7+}/O^{6+} or C^{6+}/C^{5+} were seen.

For the pseudostreamer solar wind, a collection of pseudostreamers in the years 2002–2008 made by *Borovsky and Denton* [2013] was used. Here a pseudostreamer interval is identified at 1 AU as an interval of streamer belt plasma separating two coronal hole regions with the same magnetic polarity [cf. *Borovsky and Denton*, 2013]. In general, there is no magnetic sector reversal in a pseudostreamer interval.

For the selection of the "sector reversal regions," identification purely by the electron strahl was used with ACE SWEPAM electron measurements and a knowledge of the location of the sector reversals. To gauge the properties of the electron strahl, temporal pitch angle plots of the intensity of 230 eV electrons on ACE were examined. Around a magnetic sector reversal at 1 AU, a broad region where the electron strahl drops out can be found. Just outside of that strahl dropout region there is usually a region where the strahl is very weak, intermittent, and/or intermittently bidirectional (but still weak). The authors denoted these regions as "strahl confusion zones," and these confusion zones were selected as the "sector reversal regions."

In the four-plasma categorization scheme, the pseudostreamer points will represent the parameter space of streamer belt plasma and the strahl confusion zones will represent the parameter space of sector-reversal-region plasma. Hence, it is implicitly assumed that pseudostreamer intervals at 1 AU are comprised of streamer-belt-origin plasma and that helmet streamer intervals at 1 AU are comprised of streamer-belt-origin and sector-reversal-region plasmas.

For ejecta, the *Lepping et al*. [2005] magnetic cloud collection is used. The Lepping cloud collection can be found at http://wind.gsfc.nasa.gov/mfi/mag_cloud_pub1.html. Magnetic clouds are a subset of interplanetary coronal mass ejections distinguished by enhanced magnetic fields with a slow rotation in direction, suggestive of a flux rope field configuration, low proton temperatures and low plasma beta [e.g., *Klein and Burlaga*, 1982]. As many studies have noted, only a minority of ICMEs (typically ~30%) are magnetic clouds [cf., *Bothmer and Schwenn*, 1996; *Richardson and Cane*, 2004]. The well-defined set of magnetic clouds is chosen to develop the criteria for ejecta rather than a broader collection of ICMEs, such as those compiled by *Cane and Richardson* [2003] and *Richardson and Cane* [2010]. (Such ICME collections were used by *Zhao et al*. [2009] to develop their criteria for identifying ejecta.) Broader collections of ejecta beyond clouds probably contain some data that is not truly ejecta; it is clear that the Lepping magnetic clouds are ejecta from the Sun. It will be found in section 3.1 that ejecta categorized with the scheme developed in section 2.2 will have two populations when the heavy ion charge-state ratios are examined, with one population resembling the Lepping magnetic clouds and the second population resembling nonclouds. The larger ejecta collection of *Richardson and Cane* [2010] will also be found to have this dual-population structure.

2.2. The Three-Parameter Four-Plasma Categorization Algorithm

Analogous to the *Zhao et al*. [2009] two-dimensional scheme that uses the O^{7+}/O^{6+} charge-state ratio of the solar wind, a simple two-dimensional categorization scheme that uses measurements of the proton-specific entropy S_p and the proton Alfvén speed v_A appears in Figure 3. Points from the OMNI2 data set are plotted for four collections of solar wind events described in section 1.1. Plotted in blue is v_A as a function of S_p for the Lepping collection of magnetic clouds, plotted in red is the set of unperturbed coronal hole plasma, plotted in green is the collection of pseudostreamer wind, and plotted in purple is the collection of strahl confusion zones. As can be seen, the populations tend to separate in v_A-S_p space with the sector-reversal-region plasma, the streamer-belt-origin plasma, and the coronal-hole-origin plasma forming a diagonal band. Three curves are chosen by eye to separate the points: the three curves are as follows:

$$v_A = 60\ \log_{10}(16\ S_p) \tag{2a}$$

$$v_A = 40/S_p \tag{2b}$$

$$S_p = 4\ \text{eV cm}^2 \tag{2c}$$

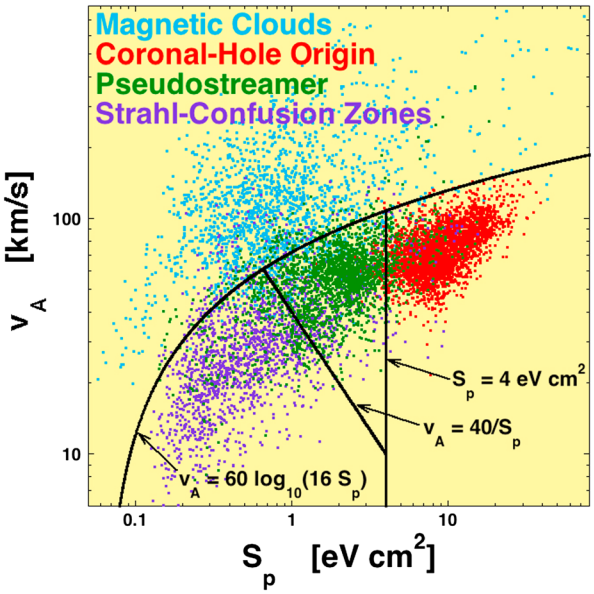

Figure 3. Hourly averaged values of solar wind data are plotted for four collections of wind types: unperturbed coronal-hole-origin wind (red), pseudostreamers (streamer-belt-origin wind, green), sector reversal regions (purple), and the Lepping magnetic clouds (blue). The four types of wind are plotted in an entropy versus Alfvén speed scheme. The black curves are given by expressions (2). The data are from OMNI2.

(where $v_A = B/(4\pi m_p n_p)^{1/2}$ is in units of km/s and $S_p = T_p/n_p^{2/3}$ is in units of eV cm^2) are drawn in black. In Table 1 the fraction of points that are categorized correctly for the two-parameter (S_p versus v_A) scheme of expressions (2a, 2b, 2c) are listed in the first column. For comparison, the accuracies of the *Zhao et al.* [2009] O^{7+}/O^{7+} versus v_{sw} scheme (Figure 2) are listed in the third column of Table 1. Here since *Zhao et al.* [2009] do not distinguish the two, the pseudostreamer and strahl confusion zone plasmas are combined into "total streamer belt plasma." And for further comparison, in the fourth column, the two plasma types are combined in the S_p versus v_A scheme (by not using expression (2b)). As can be seen by comparing the third and fourth columns in the table, the S_p versus v_A two-dimensional scheme does much better at identifying magnetic clouds and identifying streamer belt plasma than does the *Zhao et al.* [2009] scheme.

The two-parameter S_p versus v_A scheme of Figure 3 operates in two dimensions with lines and curves (expressions 2a, 2b, 2c separating the regions: this will now be extended by developing a three-parameter (S_p, v_A, T_{exp}/T_p) scheme operating in three dimensions with planes separating the regions. (Here T_{exp} is a velocity-dependent expected proton temperature.) Planes are chosen for greater mathematical simplicity in three dimensions rather than curved surfaces. Three-dimensional plots will be needed to visualize the scheme.

It is important to note in the section (as is true everywhere in the manuscript) that S_p is in units of eV cm^2, v_A is in units of km/s, and T_p and T_{exp} are in units of eV.

Several variables were explored for the third dimension and the quantity T_{exp}/T_p was chosen. Here T_p is the measured proton temperature of the solar wind and T_{exp} is the expected temperature of the protons for a given solar wind speed v_{sw} (given by expression (3)). In Figure 4 the four groups of points are plotted in two two-dimensional planes. Figure 4 (left) displays the solar wind points in v_A-S_p space (as in Figure 3) and Figure 4 (right) displays the same points in v_A-T_{exp}/T_p space. One can see that in Figure 4 (left) the four groups

Table 1. The Fraction of Time Wherein Various Categorization Schemes Get the Categorization Correct Is Listed for the Lepping Magnetic Clouds, the Unperturbed Coronal Hole Plasma, Pseudostreamer Plasma, and Strahl Confusion Zones[a]

	Two-Parameter Four-Category S_p-v_A Scheme	Three-Parameter Four-Category S_p-v_A-T_{exp}/T_p Scheme	Two-Parameter Zhao et al. O^{7+}/O^{6+}-v_{sw} Scheme	Two-Parameter Three-Category S_p-v_A Scheme	Three-Parameter Three-Category S_p-v_A-T_{exp}/T_p Scheme
Lepping magnetic clouds	83.2%	87.5%	63.5%	83.2%	87.5%
Unperturbed coronal hole	96.7%	96.9%	98.0%	96.7%	96.9%
Pseudostreamer plasma	69.5%	69.9%			
Strahl confusion zones	71.8%	72.0%			
Total streamer belt plasma			73.0%	86.7%	87.9%

[a]The *Zhao et al.* [2009] categorization scheme is based on hourly measurements of the O^{7+}/O^{6+} density ratio of the solar wind from ACE; the S_p-v_A, and S_p-v_A-T_{exp}/T_p categorization schemes are based on hourly measurements of the protons and magnetic field of the solar wind from OMNI2. The category "streamer belt plasma" is the pseudostreamer plasma plus the sector reversal regions. For the 3-category S_p versus v_A and S_p-v_A-T_{exp}/T_p schemes, the regions for sector reversal regions and streamer belt plasma are combined.

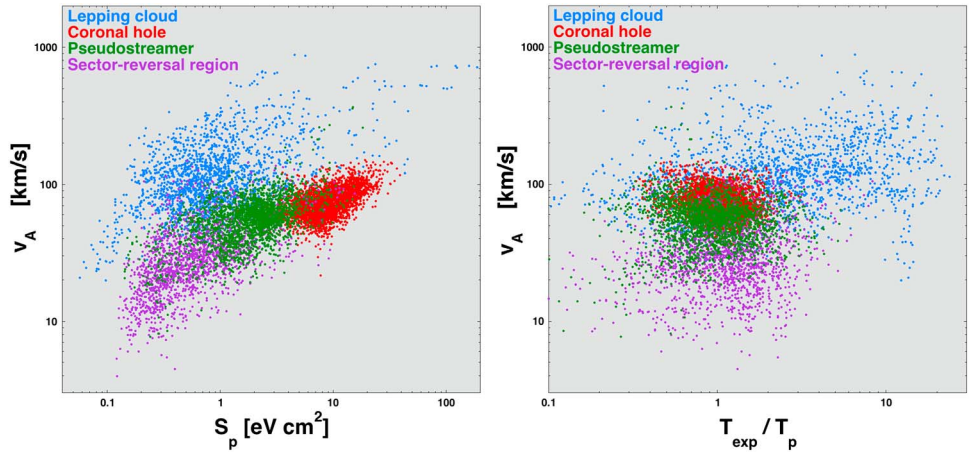

Figure 4. (left and right) Two two-dimensional views of the four collections of plasma in S_p-v_{sw}-T_{exp}/T_p space. The advantage in three dimensions of including the additional parameter T_{exp}/T_p to separate ejecta from the other populations can be seen. The data are from OMNI2.

of points are mostly separated in v_A-S_p space, but there is some overlap between the Lepping magnetic cloud points (blue) and the other three groups of nonejecta points. By using the third variable T_{exp}/T_p (Figure 4, right), much of that overlap between the Lepping magnetic clouds (blue) and the nonejecta plasma is removed.

The advantage of the variable T_{exp}/T_p is that it helps to separate ejecta from nonejecta. There are a few formulas in the literature for $T_{exp}(v_{sw})$ [e.g., *Lopez*, 1987; *Elliott et al.*, 2005, 2012; *Borovsky and Steinberg*, 2006], but a new formula is developed here from a fit of T_p to v_{sw} for nonejecta data points. In Figure 5 the measured proton temperature T_p is plotted as a function of the measured solar wind speed v_{sw} for the collections of unperturbed coronal-hole-origin solar wind (red) and the strahl confusion zones around sector reversals (purple). For these two groups of nonejecta solar wind, the data are well fit by the power law

$$T_{exp} = (v_{sw}/258)^{3.113}, \tag{3}$$

where T_{exp} is in units of eV and v_{sw} is in units of km/s.

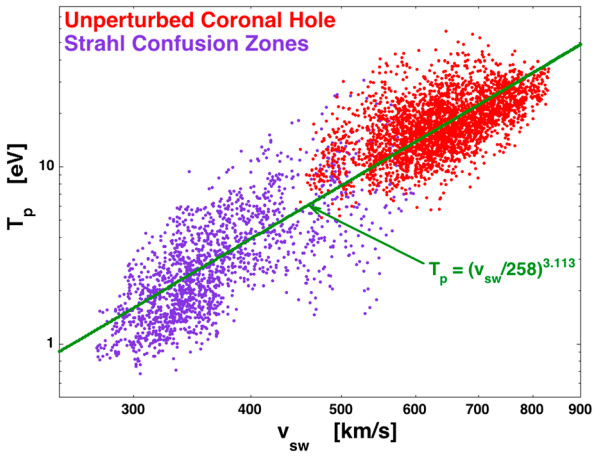

Figure 5. The proton temperature T_p is plotted as a function of the solar wind speed v_{sw} with the OMNI2 data set. The red points are the unperturbed coronal hole collection and the purple points are the strahl confusion zone collection. The green line is the fitting result $T_{exp} = v_{sw}/258)^{3.113}$.

In Figure 6 the four collections of points are plotted in three dimensions (log (S_p) versus log (v_p) versus log (T_{exp}/T_p)), and the three planes used to separate the four groups are shown. The locations and orientations of the three planes were chosen initially by eye using a visualization program that rotates the three-dimensional point plots in three dimensions. Then by trial and error the planes were shifted in location and tilted to maximize the fractional separation of the different point groups. The magenta plane separates the ejecta plasma from the three other nonejecta types of plasma. The equation for the magenta plane is as follows:

$$-3.88\ \log_{10}(S_p) + 14\log_{10}(v_A) - 0.77\ \log_{10}(T_{exp}/T_p) = 25.56. \tag{4}$$

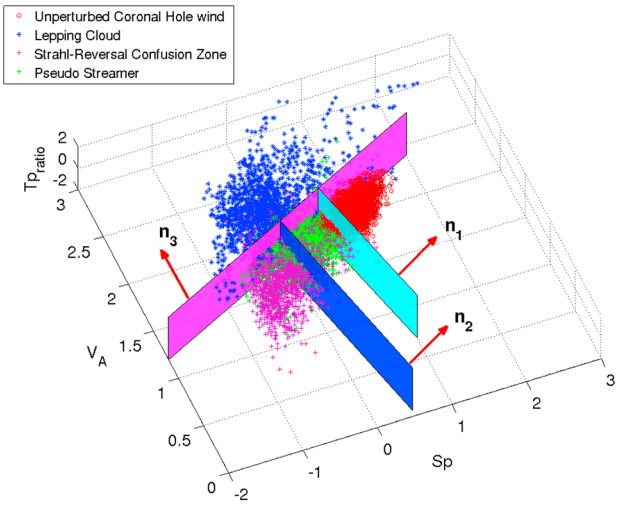

Figure 6. Four collections of different types of solar wind plasma are plotted in 3-D (S_p, v_A, $T_{pratio} = T_{exp}/T_p$) space. The blue points are the Lepping magnetic clouds, the red points are the unperturbed coronal hole wind, the green points are the pseudostreamers, and the purple points are the regions around sector reversals. The S_p, v_A, and T_{pratio} are all in log scale. The magenta plane separates the ejecta from the other three nonejecta types of plasma. The dark blue plane separates the streamer-belt-origin plasma from the sector-reversal-region plasma. The light blue plane separates the streamer-belt-origin plasma from the coronal-hole-origin plasma. The directions of the three normals to the three planes (see Appendix A) are indicated with red arrows. The data are from OMNI2.

By examining Figure 6 and using expression (4) for the magenta plane one can see that if

$$\log_{10}(v_A) > 0.277\ \log_{10}(S_p) + 0.055\ \log_{10}(T_{exp}/T_p) + 1.83, \quad (5)$$

then the magnetic cloud data points are well separated and the categorization is "ejecta." In Figure 6 the light blue plane separates the pseudostreamer point collection from the unperturbed coronal hole point collection; the equation of the light blue plane is as follows:

$$5.92\ \log_{10}(S_p) + 4\ \log_{10}(v_A) + 3.108\ \log_{10}(T_{exp}/T_p) = 10.30. \quad (6)$$

By examining Figure 6 and using expression (6) for the light blue plane one can see that if

$$\log_{10}(S_p) > -0.525\ \log_{10}(T_{exp}/T_p) - 0.676\ \log_{10}(v_A) + 1.74, \quad (7)$$

and if the categorization is not ejecta (i.e., if expression (5) is not satisfied), then the categorization is "coronal-hole-origin plasma." In Figure 6 the dark blue plane separates the sector reversal region point collection from the pseudostreamer point collection; the equation of the dark blue plane is

$$6.08\ \log_{10}(S_p) + 4\ \log_{10}(v_A) + 0.76\ \log_{10}(T_{exp}/T_p) = 6.30. \quad (8)$$

By examining Figure 6 and using expression (8) for the dark blue plane, one can see that if

$$\log_{10}(S_p) < -0.658\ \log_{10}(v_A) - 0.125\ \log_{10}(T_{exp}/T_p) + 1.04, \quad (9)$$

and if the categorization is not ejecta (i.e., if expression (5) is not satisfied), then the categorization is "sector-reversal-region plasma" based on the separation of the strahl confusion zone data points. If none of the expressions (5), (7), or (9) are satisfied, then the categorization is "streamer-belt-origin plasma" based on the pseudostreamer data points.

This categorization scheme is summarized in Table 2.

A second mathematical way to implement the categorization scheme (using the normal directions to the planes) is described in Appendix A. The mathematical scheme in the Appendix A has the advantage that it is computationally vectorizable.

Note for v_A in units of km/s the relation $v_A = 21.8\ B/n^{1/2}$ holds for B in units of nT and n in units of cm^{-3}; using this, the logarithm $\log_{10}(v_A)$ can be written $\log_{10}(v_A) = \log_{10}(21.8) + \log_{10}(B) - 0.5\ \log_{10}(n)$. Similarly, the definition $S_p = T_p/n_p^{2/3}$ yields $\log_{10}(S_p) = \log_{10}(T_p) - 0.667\ \log_{10}(n_p)$. Similarly, expression (3) enables $\log_{10}(T_{exp}) = \log_{10}(7.51 \times 10^{-8}) + 3.113\ \log_{10}(v_{sw})$. With these relations, the three logarithms $\log_{10}(v_A)$, $\log_{10}(S_p)$, and $\log_{10}(T_{exp}/T_p)$ can be rewritten in terms of n_p, T_p, B, and v_{sw}. Taking the power of 10 of both sides of expressions (5), (7), and (9), these three expressions can be rewritten as

$$Q_1 \equiv 0.841\ B\ n_p^{-0.315}\ T_p^{-0.222}\ v_{sw}^{-0.171} > 1 \quad (10a)$$

$$Q_2 \equiv 8.77 \times 10^{-11}\ T_p\ B^{1.42}\ v_{sw}^{3.44}\ n_p^{-2.12} > 1 \quad (10b)$$

$$Q_3 \equiv 0.0561\ T_p\ B^{0.752}\ v_{sw}^{0.445}\ n_p^{-1.14} < 1 \quad (10c)$$

Table 2. The Three-Parameter Categorization Scheme for the Four Types of Solar Wind Plasma[a]

	Is Expression (5) or Expression (10a) Satisfied?	Is Expression (7) or Expression (10b) Satisfied?	Is Expression (9) or Expression (10c) Satisfied?
Ejecta	Yes		
Coronal-hole-origin plasma	No	Yes	
Sector-reversal-region plasma	No		Yes
Streamer-belt-origin plasma	No	No	No

[a]If a cell is blank, the answer in that cell is irrelevant.

where n_p is in units of cm^{-3}, T_p is in units of eV, B is in units of nT, and v_{sw} is in units of km/s. If desired, the three expressions 10a, 10b, 10c can be used in place of expressions (5), (7), and (9) for implementing the categorization scheme (see Table 2), a simpler but less visualizable scheme.

Accuracy of the four-plasma categorization scheme can be judged via Tables 1 and 3. For the four collections of known solar wind data used to develop the scheme, in Table 1, the fraction of points from each collection that is categorized correctly for the three-parameter S_p-v_A-T_{exp}/T_p scheme of Table 2 is listed in the second column. For comparison the accuracies of the *Zhao et al.* [2009] O^{7+}/O^{7+} versus v_{sw} scheme (Figure 2) are listed in the third column of Table 1. Here the pseudostreamer and sector-reversal-region plasmas are combined into "total streamer belt plasma." And for further comparison, in the last column the two plasma types are combined in the S_p-v_A-T_{exp}/T_p scheme (by not utilizing expression (9) or expression (1c)). As can be seen in Table 1, the three-parameter scheme does much better at identifying known magnetic cloud intervals than the prior Zhao et al. two-parameter scheme. By comparing the first and second columns of Table 1, it is seen that the three-parameter S_p-v_A-T_{exp}/T_p four-plasma scheme does a better job at identifying known clouds and known sector-reversal-region plasma than does the two-parameter S_p-v_A four-plasma scheme.

Having developed the three-parameter four-plasma categorization scheme using certain selected solar wind intervals, the scheme is now tested against other collections of solar wind data. In Table 3 the results of categorizing 17 different collections of solar wind into the four plasma types is shown. The second column of Table 3 lists the number of hours in each data collection. The four collections of points that were used to develop the scheme are collections 1–4 in the table (see section 2.1). Collection 5, which is a collection of cloud and noncloud ejecta, comes from the tables of *Richardson and Cane* [2010]. Collection 6, which is a collection of cloud and noncloud ejecta, comes from the appendix of *Jian et al.* [2006]. The S_p-v_A-T_{exp}/T_p scheme identifies 63.3% of the Richardson and Cane ICME collection as ejecta and identifies 69.4% of the Jian magnetic obstacle collection as ejecta. As noted in section 2.1, it may be the case that not all of the points in those two collections are truly ejecta. Note that the *Zhao et al.* [2009] O^{7+}/O^{6+}-v_{sw} scheme identifies only 49.7% of the points in the Richardson and Cane ICME collection as ejecta, even though that scheme was created using a similar [*Cane and Richardson* [2003]] ICME collection. Collection 7 are ACE bidirectional-electron-strahl events gathered by the authors; the events were screened to eliminate bidirectional strahls associated with passing interplanetary shocks; bidirectional strahl intervals are associated with closed field line regions in the solar wind (ejecta) but also could be associated with shocks beyond 1 AU [*Steinberg et al.*, 2005] including perhaps the Jovian bow shock. Collection 8 are helmet streamers used in the study of *Borovsky and Denton* [2013]. Collection 9 is a collection of ninety-three 27 day repeating high-speed stream-driven storms used in the study of *Borovsky and Denton* [2010b]. Collection 10 is a collection of 24 long-period geomagnetic calms before high-speed stream-driven storms from the study of *Borovsky and Denton* [2009]. Collections 11 and 12 are the early and the later portions of the trailing edges of 27 high-speed streams collected by the authors using OMNI2 and ACE spacecraft data. As the velocity declines with time in the trailing edge, a point can be found where the time derivative of the solar wind velocity suddenly changes; this point is statistically colocated with the minimum of the solar wind density and the minimum magnetic field strength. Statistically, there is also a large vorticity (velocity shear) colocated with this velocity derivative change. It is likely that this point marks the stream interface between coronal hole plasma and streamer belt plasma in the trailing edge of the high-speed stream. Collection 11 is the first part of the trailing edge up to the occurrence of the velocity derivative change (expected to be coronal-hole-origin plasma) and Collection 12 is the second part of the trailing edge after the occurrence of the velocity derivative change (expected to be streamer belt origin and

Table 3. The S_p-v_A-T_{exp}/T_p Scheme Is Used to Categorize 17 Different Collections of Solar Wind Data Into Four Types[a]

	Data Collection	Hours of Data	1 Ejecta	2 Coronal-Hole-Origin Plasma	3 Streamer-Belt-Origin Plasma	4 Sector-Reversal-Region Plasma	Expected Result	Fraction Categorized Correctly
1	Lepping magnetic clouds	1926	87.5%	1.1%	4.6%	6.8%	1	87.5%
2	Unperturbed coronal hole	3049	0.7%	96.9%	2.4%	0.0%	2	96.9%
3	Pseudostreamers	2275	10.7%	4.5%	69.9%	14.9%	3	69.9%
4	Strahl confusion zones	1740	5.8%	2.0%	20.2%	72.0%	4	72.0%
5	Richardson + Cane ejecta	6168	63.3%	7.0%	14.4%	15.3%	1	63.3%
6	Jian magnetic obstacles	4547	69.4%	3.4%	14.2%	13.0%	1	69.4%
7	Bidirectional strahl intervals	1212	48.5%	9.2%	22.4%	19.9%	1 + ?	?
8	Helmet streamers	15455	8.6%	0.9%	42.5%	48.0%	3 + 4	90.5%
9	High-speed stream-driven storms	6251	10.1%	78.3%	9.4%	2.2%	2 + 1	88.4%
10	Calms before the storms	5892	10.2%	6.0%	39.5%	44.3%	3 + 4	83.7%
11	Trailing edges before the velocity bend	1669	1.0%	75.3%	23.6%	0.1%	2	75.3%
12	Trailing edges after the velocity bend	2974	4.4%	7.2%	59.9%	28.5%	3 + 4	88.4%
13	>850 km/s wind	227	59.5%	40.5%	0.0%	0.0%	1 + ?	59.5%
14	Sustained ortho-Parker-spiral intervals	4981	17.2	11.2	40.3	31.3	?	
15	Sustained out-of-ecliptic intervals	4496	43.1	5.6	24.1	27.2	?	
16	Sustained radial field intervals	5287	8.0	29.3	15.5	47.1	?	
17	All data in OMNI2	277026	12.9%	25.2%	41.7%	20.2%		

[a]The fraction of each plasma type obtained for each collection is shown in the table. The expected category (if known) is shown, and the final column is the fraction of points of each collection that are categorized "correctly." The OMNI2 data set with 277,026 h categorized is used.

sector-reversal-region plasma). Collection 13 are all the data in OMNI2 that have an hourly averaged value of v_{sw} that is greater than 850 km/s. The $v_{sw} > 850$ km/s collection has a median speed of 910 km/s and a mean speed of 928 km/s. These data points are from impulsive events where the solar wind velocity typically rises quickly to well above 850 km/s and then rapidly decays back to lower speeds; they are most likely high-velocity ejecta plasma with some swept-up nonejecta plasma ahead of the ejecta. The sustained ortho-Parker-spiral collection (14) are all the data in OMNI2 in intervals 3 h or longer where the IMF longitude stays in the range 70°–90° from the Parker-spiral direction, and the IMF latitude is within 30° of the ecliptic plane; not enough is known about ortho-Parker-spiral solar wind to know what plasma type to expect. The sustained out-of-ecliptic collection (15) are all the data in OMNI2 in intervals 3 h or longer where the IMF latitude is greater than 60° of the ecliptic plane; this category should contain ejecta [cf. *Burlaga et al.*, 1981; *Borovsky*, 2010], but it is not known what else. (Indeed, 43% of these intervals occur in solar wind that is categorized as ejecta; it is prevalent in ejecta since ejecta is only occurring 12.9% of the time, as indicated in the last line of Table 3. However, more than half of all sustained out-of-ecliptic intervals are occurring in solar wind that is categorized as either streamer belt or sector reversal region.) Collection 16 is of sustained radial magnetic field intervals of solar wind wherein the magnetic latitude and magnetic longitude both stay within 15° of radial for 3 h or more. Not enough is known about radial field intervals to know what to expect for the types of plasma: radial fields have been associated with the legs of coronal mass ejections and with rarefactions [e.g., *Neugebauer et al.*, 1997; *Gosling and Skoug*, 2002; *Murphy et al.*, 2002; *Riley and Gosling*, 2007], particularly with streamer belt origin wind in rarefactions [*Orlove et al.*, 2013]. The final collection (17) is all OMNI2 data that is categorized. The second from last column in Table 3 is the expected answer for the categorization, i.e., which type of plasma should be dominant for each type of collection. The final column is the fraction of the points that are "correctly" categorized for each collection. As can be seen in the final column of Table 3, the fractions correctly categorized are high.

The potential effects of interplanetary shocks on the categorization scheme are examined in Table 4. For 108 interplanetary shocks, 2 h of data upstream of each shock and 2 h of data downstream of each shock are collected, and the downstream collection is compared with the upstream collection. In Table 4 the mean values of the proton-specific entropy S_p, the proton Alfvén speed v_A, and the temperature ratio T_{exp}/T_p upstream and downstream of the 108 shocks are listed. The final column is the ratio of the downstream average to the upstream average. The typical changes are by factors of about 2. S_p tends to increase by about a factor of 2, making the plasma look more coronal hole like in the categorization scheme; v_A tends to increase by about a factor of 2 making the plasma look more ejecta like; T_{exp}/T_p tends to decrease by about a factor of 2 making the plasma look less ejecta like. These factors of 2 are modest compared with the

Table 4. For 108 (Forward) Interplanetary Shocks (From the ACE Lists of Disturbances and Transients http://www.ssg.sr.unh.edu/mag/ace/ACElists/obs_list.html), the Mean Values of the Three Quantities Used in the Categorization Scheme are Listed for the Preshock Plasma and the Postshock Plasma[a]

	Mean Value Preshock	Mean Value Postshock	Ratio Postshock to Preshock
S_p	2.5 eV cm^2	5.4 eV cm^2	2.20
v_A	56 km/s	86 km/s	1.54
T_{exp}/T_p	1.4	0.79	0.56

[a]For each shock, 2 h of data are used in the preshock region and 2 h of data are used in the postshock region.

orders-of-magnitude ranges of the three values (cf. Figure 3). The conclusion is that interplanetary shocks will not severely impact the categorization of the solar wind plasma. Of course points that lie near the planes (cf. Figure 6) can change categorizations owing to the passage of a shock. It is left as a judgment call for the reader to decide whether or not to implement a correction scheme for interplanetary shocks.

Occasionally, very fast solar wind is seen, with speeds >850 km/s [cf. *Skoug et al.*, 2004; *Liu et al.*, 2014]. This very fast wind is almost certainly ejecta (with perhaps some nonejecta plasma ahead of the ejecta that is pushed up to very high speeds). This very high speed wind often has a very high proton-specific entropy. One might worry that this fast ejecta would be mistaken for coronal-hole-origin plasma by the categorization scheme and one might consider overruling the categorization scheme and declaring any plasma with $v_{sw}>850$ km/s as "ejecta." An examination of the 227 h of data in OMNI2 with $v_{sw}>850$ km/s finds that the scheme categorizes this as ejecta 59.5% of the time and as coronal-hole-origin plasma 40.5% of the time (see line 13 of Table 3). If there is swept-up nonejecta plasma ahead of the ejecta, it is not likely to be of coronal hole origin 100% of the time; overriding the categorization scheme might be justified.

3. Properties of the Four Solar Wind Plasmas

In Figure 7, 40 days of OMNI2 solar wind velocity v_{sw} and the IMF longitude (in GSE coordinates) are plotted. This is an interval in 2006 of solar wind from the declining phase of the solar cycle with well-developed (but weak) repeating high-speed streams. The results of the four-plasma categorization scheme are indicated

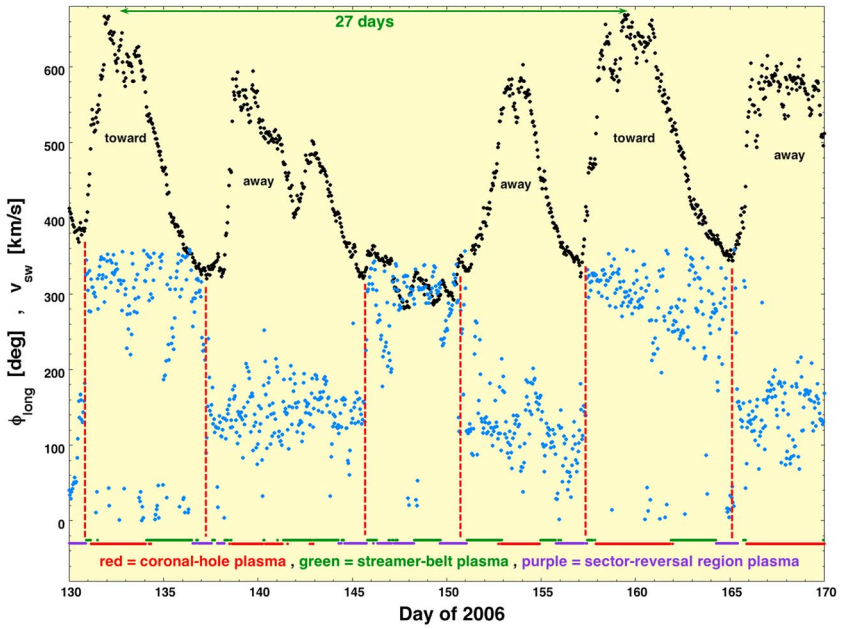

Figure 7. Using 1 h OMNI2 data, 40 days of categorized solar wind is plotted late in the declining phase of the solar cycle. The black points are the solar wind speed v_{sw}, the blue points are the IMF GSE longitude, and the band of colored points indicates the result of the plasma categorization (see labels). The vertical red dashed lines are the locations of magnetic sector reversals. The green horizontal arrow marks the solar rotation period of 27 days.

Table 5. Mean Values for Various Plasma Parameters in the Four Types of Solar Wind Plasma at 1 AU[a]

	Ejecta	Coronal-Hole-Origin Plasma	Streamer-Belt-Origin Plasma	Sector-Reversal-Region Plasma	All Solar Wind
Plasma age (h)	100	75	103	123	100
n_p (cm^{-3})	6.8	3.5	6.3	12.0	6.8
T_p (eV)	7.7	18.4	8.2	3.0	9.7
B (nT)	11.0	6.1	5.7	4.6	6.3
v_{sw} (km/s)	434	567	409	342	438
Log_{10} (O^{7+}/O^{6+})	-0.495	-1.13	-0.754	-0.446	-0.766
Log_{10} (C^{6+}/C^{5+})	0.053	-0.263	0.038	-0.067	-0.059
Fe/O	0.11	0.058	0.076	0.090	0.077
Log_{10} (S_α)	2.1	2.7	2.1	1.4	2.1
P_{type}	0.95	3.1	1.4	0.029	1.7
α/p	0.051	0.042	0.040	0.024	0.038
$\delta B/B$	0.24	0.46	0.40	0.38	0.39
M_A	4.4	8.3	8.6	13.1	8.8
P_{ram} (nPa)	2.6	2.2	2.1	2.7	2.3
Kp	2.7	2.9	1.8	1.3	2.2
β_p	0.13	0.75	0.74	0.98	0.71
v_A (km/s)	110	73	51	31	61
c/ω_{pi} (km)	114	133	99	73	104
r_{gi} (km)	24	75	55	43	54

[a]For O^{7+}/O^{6+}, C^{6+}/C^{5+}, Fe/O, S_α, and P_{type}, the 1998–2011 ACE data set was used; for all other quantities, the 1963–2012 OMNI2 data set was used. For logarithmic quantities, the mean value of the logarithm is given. The quantity c/ω_{pi} is the ion-inertial length and r_{gi} is the thermal ion gyroradius.

by the colored points, with red indicating coronal-hole-origin plasma, green indicating streamer-belt-origin plasma, and purple indicating sector-reversal-region plasma. In this interval, no plasma was categorized as ejecta. The red vertical dashed lines indicate the locations of magnetic sector reversals, as indicated by the IMF longitude and confirmed with the electron strahl on ACE. Note in Figure 7 that the "sector-reversal-region plasma" (purple) tends to be found around the locations of the sector reversals: recall that the categorization of sector-reversal-region plasma comes from an examination of S_p, v_A, and T_{exp}/T_p without any examination of the IMF direction.

In Figure 7 the "toward" or "away" magnetic sector for each high-speed stream is indicated in black. Typically, the sector reverses from one high-speed stream to the next. Note, however, the two consecutive streams centered on days ~140 and ~153: they are both away-sector high-speed streams. Ordinarily, the streamer belt plasma between these two streams would be classified as pseudostreamer plasma, and ordinarily that pseudostreamer plasma would not contain any sector reversals. However, the interval of streamer belt plasma from day 143 to day 152 contains two clear sector reversals. As suggested by a reviewer, this may be a case where a spacecraft connection is skimming across the sector reversal without reaching the coronal hole plasma on the other side. The categorization scheme finds that these paired sector reversals have sector-reversal-region plasma around them.

To gauge the general properties at 1 AU of the four types of solar wind plasma, in Table 5 the mean values of a number of common plasma parameters at 1 AU are listed for the four categorizations of the solar wind plasma plus for all solar wind. Some values are statistically similar in the different types of plasma, some values are different. The plasma age is the time of flight of the plasma from the Sun to 1 AU.

3.1. Properties Involved in Other Solar Wind Categorization Schemes

In Figure 8 the occurrence distributions of $\log_{10}$ (O^{7+}/O^{6+}), of P_{type}, and of v_{sw} for the four categorizations of the solar wind plasma are plotted. These three quantities are utilized in other solar wind categorization schemes. In Figure 8 (top) the charge-state density ratio O^{7+}/O^{6+} (from ACE SWICS) is examined. This is a key parameter of the *Zhao et al.* [2009] categorization scheme (cf. Figure 2). As can be seen, the O^{7+}/O^{6+} density ratios are systematically different in the three nonejecta types of plasma, although there is considerable overlap of the occurrence distributions in the figure. Because of this trend the O^{7+}/O^{6+} ratio can be used to separate streamer-belt-origin plasma from coronal-hole-origin plasma [cf. *Zurbuchen et al.*, 2002].

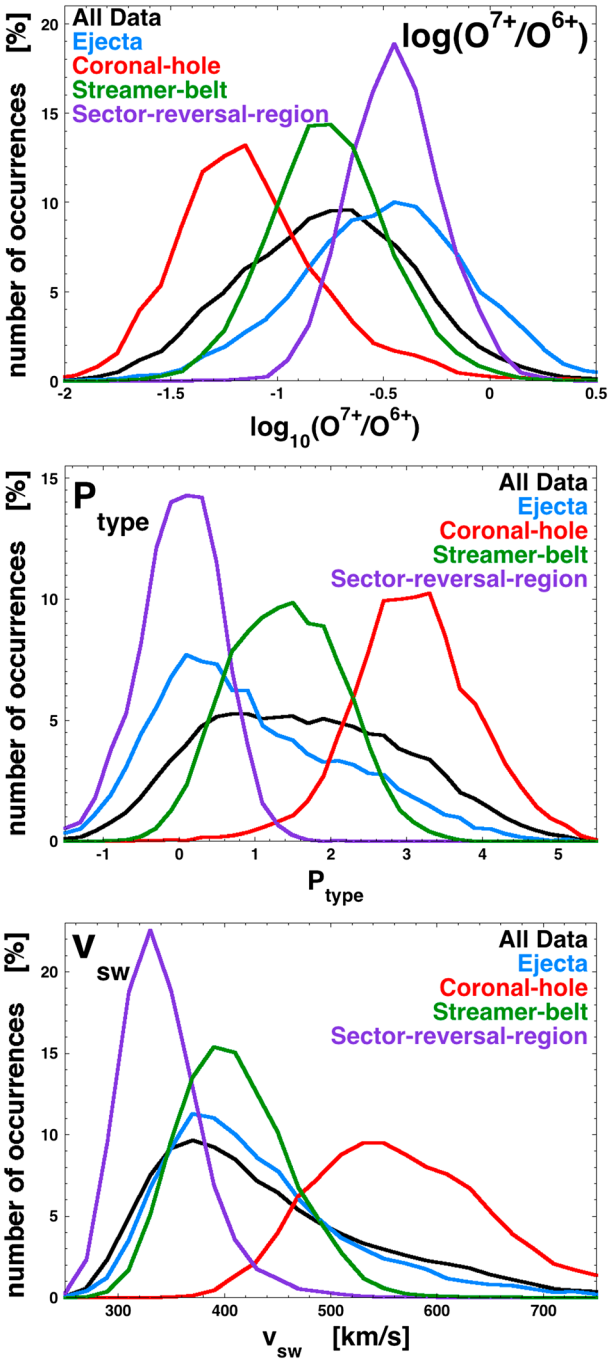

Figure 8. For the four categorizations of plasmas, the distributions of values of three parameters used in other categorization schemes are plotted. The parameters are (top) $\log_{10}(O^{7+}/O^{6+})$ (from ACE), (middle) P_{type} (from ACE), and (bottom) v_{sw} (from OMNI2). The blue curves are for ejecta, the red curves are for coronal-hole-origin plasma, the green curves are for streamer-belt-origin plasma, the purple curves are for sector-reversal-region plasma, and the black curves are from the full data set (all available data).

In Table 5 the mean values of $\log_{10}(O^{7+}/O^{6+})$ are monotonic going from coronal-hole-origin plasma to streamer-belt-origin plasma to sector-reversal-region plasma in agreement with Figure 8: this is not so for the mean values of $\log_{10}(C^{6+}/C^{5+})$ in Table 5. This carbon-oxygen difference is explored further in Figure 9 and in Table 6. In Figure 9 the O^{7+}/O^{6+} density ratio is plotted as a function of S_p on the left for the four categories of plasma and C^{6+}/C^{5+} is plotted as a function of S_p on the right for the four categories of plasma: in the plot the C^{6+}/C^{5+} values are shifted to the right by a factor of 1000 (i.e., they are plotted as a function of $1000S_p$). As can be seen for the O^{7+}/O^{6+} values, there is an anticorrelation between O^{7+}/O^{6+} and S_p that holds for all four plasma populations, although there is appreciable scatter in the ejecta population. (See *Pagel et al.* [2004] for a discussion of the O^{7+}/O^{6+}-S_p anticorrelation.) A power law fit to the data in Figure 9 finds the relationship $O^{7+}/O^{6+} \approx 0.26\ S_p^{-0.59}$ for the three nonejecta plasmas, with ejecta having greater scatter in the data. This mathematical relation is listed in the last column of Table 6 and the coherence of the relation between O^{7+}/O^{6+} and S_p in the four plasma types is indicated in Table 6. A similar fit between O^{7+}/O^{6+} and S_α that holds for coronal-hole-origin plasma, streamer-belt-origin plasma, and sector-reversal-region plasma is $O^{7+}/O^{6+} \approx 1.1\ S_\alpha^{-0.42}$; this is also listed in Table 6. The case is different for the C^{6+}/C^{5+} values in Figure 9; the anticorrelation holds for coronal-hole-origin plasma and streamer-belt-origin plasma (see Table 6), but another relation between C^{6+}/C^{5+} and S_p applies for the ejecta and the sector-reversal-region plasma. A power law fit for coronal-hole-origin plasma and streamer-belt-origin plasma yields $C^{6+}/C^{5+} \approx 1.5\ S_p^{-0.48}$ (listed in Table 6): a fit for ejecta and sector-reversal-region plasma was not attempted. A similar fit between C^{6+}/C^{5+} and S_α that holds for coronal-hole-origin plasma and streamer-belt-origin plasma is $C^{6+}/C^{5+} \approx 3.9\ S_\alpha^{-0.30}$; this is also listed in Table 6.

In Figure 10 the values of C^{6+}/C^{5+} are plotted as a function of O^{7+}/O^{6+} for the four categories of plasma. There is a strong

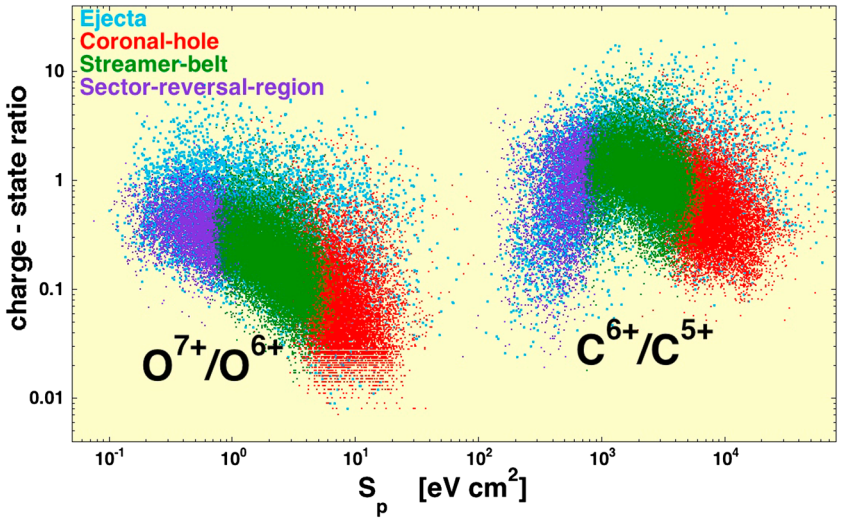

Figure 9. The relations of the charge-state density ratios C^{6+}/C^{5+} and O^{7+}/O^{6+} at 1 AU to the proton-specific entropy $S_p = T_p/n_p^{2/3}$ is examined for the four types of solar wind plasma. The data are from ACE.

correlation between C^{6+}/C^{5+} and O^{7+}/O^{6+} for coronal-hole-origin plasma and streamer-belt-origin plasma (this is indicated in Table 6) but a strong low-C^{6+}/C^{5+} deviation from that trend for ejecta and for sector-reversal-region plasma. The deviation argues that sector-reversal-region plasma may be produced by a different mechanism from coronal-hole-origin plasma and streamer-belt-origin plasma (see also Figure 9). The power law fit $C^{6+}/C^{5+} \approx 3.7\ (O^{7+}/O^{6+})^{0.71}$ holds for coronal-hole-origin plasma and streamer-belt-origin plasma in Figure 10 (see Table 6); this argues that the production of coronal-hole-origin plasma and streamer-belt-origin plasma be via a similar mechanism or from a similar location on the Sun. Note that the values of C^{6+}/C^{5+} relative to O^{7+}/O^{6+} are lower than expected for ionization equilibrium: the data in Figure 2 of *Landi et al.* [2012] predicts $C^{6+}/C^{5+} \approx 14\ O^{7+}/O^{6+}$ for the range of O^{7+}/O^{6+} values in Figure 10. For coronal hole plasma and streamer belt plasma the typical values of C^{6+}/C^{5+} in Figure 10 are more than a factor of 2 lower than 14 O^{7+}/O^{6+}: for sector-reversal-region plasma and ejecta they are much more than a factor of 2 lower.

In Figure 10 the points that are categorized as ejecta are difficult to see, plotted under the other points. The ejecta-categorized points are replotted as C^{6+}/C^{5+} versus O^{7+}/O^{6+} by themselves in Figure 11 (top). In Figure 11 (top), two distinct populations of points can be seen: the first population follows the trend of the $C^{6+}/C^{5+} \approx 3.7\ (O^{7+}/O^{6+})^{0.71}$ trend of the coronal hole plasma and streamer belt plasma and the second population deviates downward with very low values of C^{6+}/C^{5+}. In Figure 11 (middle) the Lepping-magnetic cloud collection is plotted in C^{6+}/C^{5+} versus O^{7+}/O^{6+} space. Here it is seen that the magnetic clouds occupy only the second population (with low C^{6+}/C^{5+} values). In Figure 11 (bottom), the Richardson and Cane collection of ejecta (from the tables of *Richardson and Cane* [2010]) are plotted in C^{6+}/C^{5+} versus O^{7+}/O^{6+}

Table 6. This Table Indicates in Which Solar Wind Plasmas a Simple (Power Law) Mathematical Relationship Holds Among Values of the Specific Entropies S_p and S_α and the Charge-State Density Ratios O^{7+}/O^{6+} and C^{6+}/C^{5+a}

	Ejecta	Coronal-Hole-Origin Plasma	Streamer-Belt-Origin Plasma	Sector-Reversal-Region Plasma	Approximate Mathematical Relationship
$S_\alpha \leftrightarrow S_p$	yes	yes	yes	yes	$S_\alpha \approx 57 S_p^{1.1}$
$O^{7+}/O^{6+} \leftrightarrow S_p$	yes	yes	yes	no	$O^{7+}/O^{6+} \approx 0.26\ S_p^{-0.59}$
$O^{7+}/O^{6+} \leftrightarrow S_\alpha$	yes	yes	yes	no	$O^{7+}/O^{6+} \approx 1.1\ S_\alpha^{-0.42}$
$C^{6+}/C^{5+} \leftrightarrow S_p$	yes	yes	no	no	$C^{6+}/C^{5+} \approx 1.5\ S_p^{-0.48}$
$C^{6+}/C^{5+} \leftrightarrow S_\alpha$	yes	yes	no	no	$C^{6+}/C^{5+} \approx 3.9\ S_\alpha^{-0.30}$
$C^{6+}/C^{5+} \leftrightarrow O^{7+}/O^{6+}$	yes	yes	no	no	$C^{6+}/C^{5+} \approx 3.7\ (O^{7+}/O^{6+})^{0.71}$

[a]The power law formulas in the last column are least squares linear regression fits in log-log space.

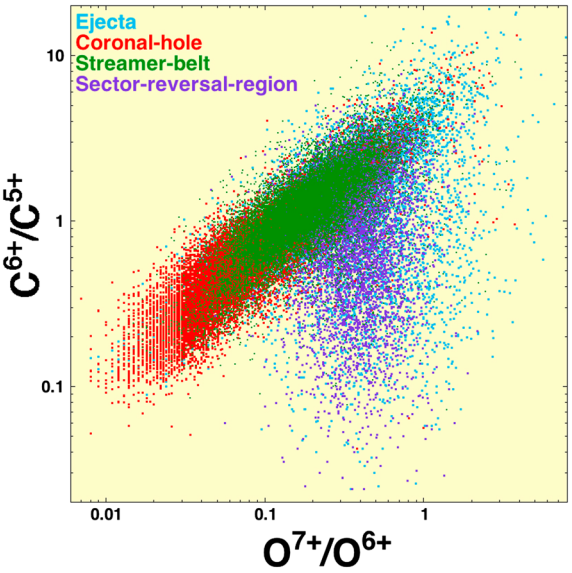

Figure 10. The relationship between the charge-state density ratios C^{6+}/C^{5+} and O^{7+}/O^{6+} at 1 AU is examined for the four types of solar wind plasma. The data are from ACE.

space. Note in Figure 11 (bottom) that this Richardson and Cane ejecta collection contains both populations, as does the ejecta categorization in Figure 11 (top): the low C^{6+}/C^{5+} population that matches the Lepping magnetic clouds and first population that follows the $C^{6+}/C^{5+} \approx 3.7(O^{7+}/O^{6+})^{0.71}$ trend.

Figure 12 contains a similar examination of the sector-reversal-region categorization. In Figure 12 (top) the points that are categorized as sector-reversal-region plasma are plotted in C^{6+}/C^{5+} versus O^{7+}/O^{6+} space, and in Figure 12 (bottom) the points of the collection of strahl confusion zones are plotted in C^{6+}/C^{5+} versus O^{7+}/O^{6+} space. There is less of a two-population trend for the sector reversal regions (Figure 12) than there is for ejecta (Figure 11). The points that are categorized as sector reversal region (and the strahl confusion zones) follow more the population occupied by the Lepping magnetic clouds than the population that follows the $C^{6+}/C^{5+} \approx 3.7(O^{7+}/O^{6+})^{0.71}$ trend.

In Figure 8 (middle), the occurrence distribution of the plasma-type parameter P_{type} (expression (1)) evaluated with measurements from ACE is plotted for the four categories of solar wind plasma. The parameter P_{type} was used in the *Borovsky and Denton* [2014] categorization. Comparing Figures 8 (top) and 8 (middle), it is seen that the P_{type} distributions have less overlap than the log (O^{7+}/O^{6+}) distributions for the three categories, coronal-hole-origin plasma, streamer-belt-origin plasma, and sector-reversal-region plasma. P_{type} involves log (S_p) and log (S_α), which are correlated with each other and involves $-$log (O^{7+}/O^{6+}) and $-$log (C^{6+}/C^{5+}), which are correlated with each other and with log (S_p) and log (S_α) strongly anticorrelated with log (O^{7+}/O^{6+}) and log (C^{6+}/C^{5+}). In a sense log (S_p), log (S_α), $-$log (O^{7+}/O^{6+}), and $-$log (C^{6+}/C^{5+}) are all measures of the transition from coronal-hole-origin plasma to streamer-belt-origin plasma to sector-reversal-region plasma, but by using P_{type}, you are using four independent measurements of that transition and the statistical (measurement) noise is smaller by combining the four measurements. (Cf. equation (1) of *von Steiger et al.* [2010] where the charge-state ratios O^{7+}/O^{6+} and C^{6+}/C^{5+} are combined to produce a better measurement.) The parameter P_{type} separates coronal-hole-origin plasma from streamer-belt-origin plasma from sector-reversal-region plasma better than O^{7+}/O^{6+} does; however, P_{type} has the same disadvantage that it is not available for most spacecraft data sets.

In Figure 8 (bottom) the occurrence distribution of the solar wind speed v_{sw} (from OMNI2) is plotted for the four categories of solar wind plasma. Like P_{type}, the speed v_{sw} does a good job of separating coronal-hole-origin plasma from streamer-belt-origin plasma from sector-reversal-region plasma. But using only v_{sw} to select fast wind versus slow wind does not exclude ejecta from the categorization. In Figure 13 the fraction of occurrence of the four types of plasma is plotted as a function of the solar wind speed v_{sw}. At low speeds ($<$ 300 km/s in the figure) the solar wind is dominated by sector-reversal-region plasma (purple curve). For speeds of 300–500 km/s, streamer-belt-origin plasma occurs about 50% of the time, with substantial amounts of sector-reversal-region plasma, coronal-hole-origin plasma, and ejecta getting into the 300–500 km/s selection. In the range 500 km/s–800 km/s, Figure 13 indicates that coronal-hole-origin plasma (red curve) fractionally dominates the solar wind, with ejecta occurring about 10% of the time. At very high speeds (which are rare), ejecta categorization is strong. Hence, a separation of the solar wind into fast wind and slow wind results in mostly coronal-hole-origin plasma in the fast wind category and a substantial mix of plasmas in the slow wind category.

3.2. Alpha Particles, Fe/O, Proton Beta, and Fluctuations in the Four Plasma Types

In Figure 14 the occurrence distributions of four plasma parameters (the alpha-to-proton density ratio α/p, the iron-to-oxygen abundance ratio Fe/O, the alpha-particle-specific entropy S_α, the proton beta β_p, and the normalized amplitude of magnetic field fluctuations $\delta B/B$) are plotted for the four types of solar wind plasma.

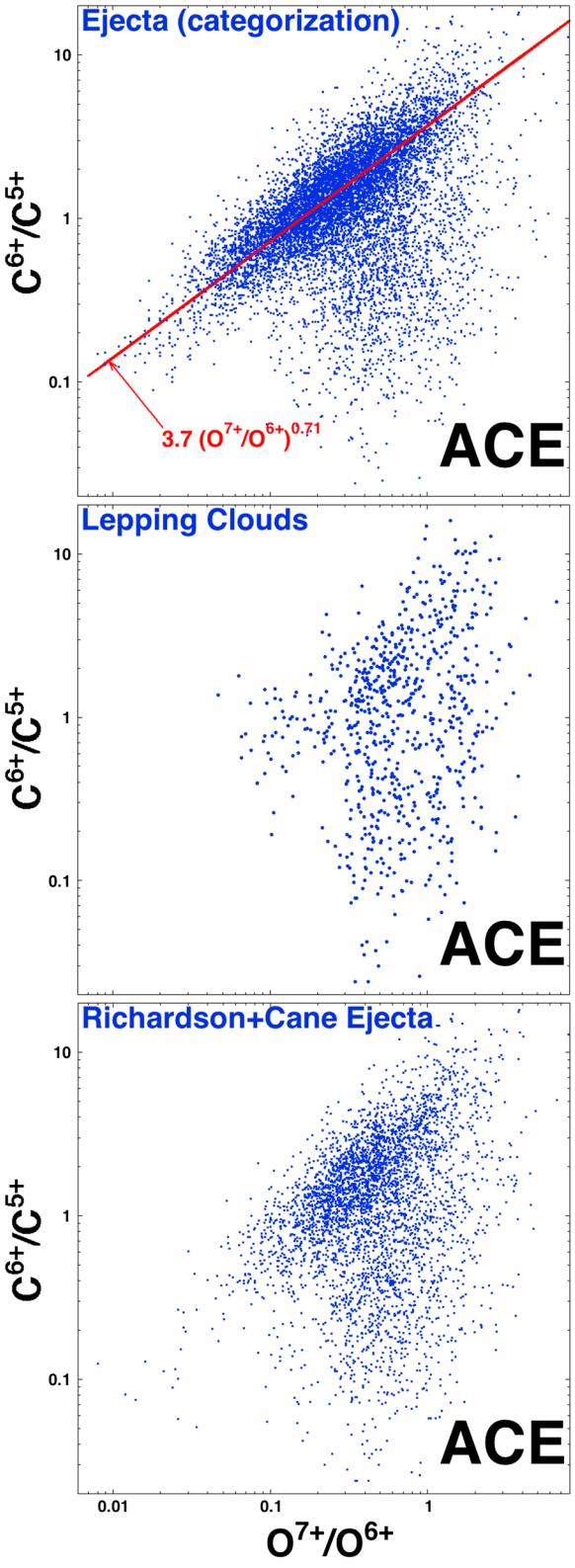

Figure 11. Similar to Figure 10, (top) the points categorized as ejecta are plotted by themselves and for comparison (middle) the Lepping magnetic cloud collection of points is plotted, and (bottom) the Richardson and Cane collection of ICME points is plotted.

In Figure 14 (top) the alpha-to-proton density ratio of the solar wind is binned in OMNI2 for the four categorizations of the solar wind. The low α/p ratio for the sector-reversal-region plasma (purple curve) stands out. (See also *Borrini et al*. [1981], *Gosling et al*. [1981], and *Suess et al*. [2009] for observations and discussion of low α/p density ratios at sector reversals.) Low helium abundance is seen in the cores of streamers at the Sun [cf. *Raymond et al*., 1997]. Note that the distribution of α/p values for streamer-belt-origin plasma (green curve) is about the same as it is for coronal-hole-origin plasma (red) and ejecta (blue), indicating that the sector-reversal-region plasma (chosen by its values of S_p, v_A, and T_p) is indeed statistically different from the ordinary streamer-belt-origin plasma.

In Figure 14 (second panel) the occurrence distribution of the logarithm of the iron to oxygen density ratio Fe/O from ACE is plotted for the four types of solar wind plasma. The Fe/O ratio is lowest on average in coronal-hole-origin plasma (red curve) and highest in ejecta (blue) and sector-reversal-region plasma (purple). The low Fe/O values of coronal hole wind are well known [*Wurz et al*., 1999; *Aellig et al*., 1999b; *McIntosh et al*., 2011]. Here sector-reversal-region plasma is found to have a higher Fe/O abundance ratio on average than does streamer-belt-origin plasma (see also *Aellig et al*. [1999a], where higher Fe/O ratios were seen for very slow solar wind); this may reflect the higher Fe/O ratios seen at the core of streamers at the Sun compared to their edges [cf. *Raymond et al*., 1997; *Parenti et al*., 2000] or the enhanced iron density in streamers [*Habbal et al*., 2007]. Note that the distribution of values of the abundance ratio Fe/O is similar in the ejecta and sector-reversal-region plasma, possibly implying a similar birth mechanism for those two types of plasma.

In Figure 14 (third panel) the occurrence distribution of the logarithm of the alpha-particle specific entropy $S_\alpha = T_\alpha/n_\alpha^{2/3}$ from ACE is plotted for the four categorizations of the solar wind plasma. The alpha-particle-specific entropy can also be used to separate coronal-hole-origin plasma from streamer-belt-origin plasma from sector-reversal-region plasma.

In Figure 15 the relationship between the alpha-particle-specific entropy S_α and the proton-specific entropy S_p is examined. S_α is

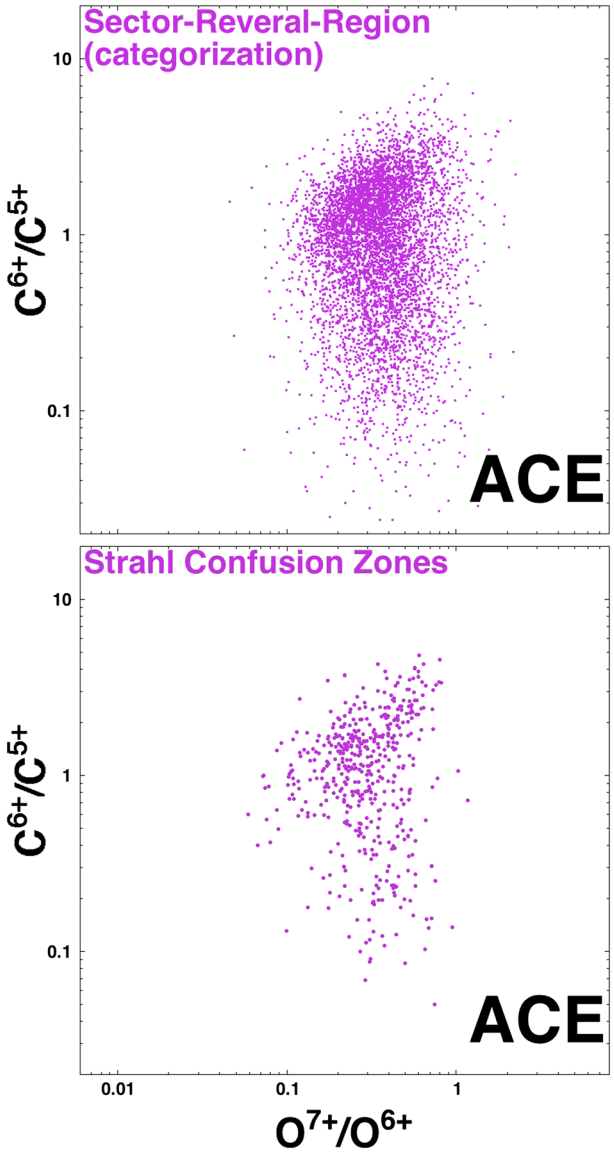

Figure 12. Similar to Figure 10, (top) the points categorized as sector-reversal-region plasma are plotted by themselves and for comparison (bottom) the strahl-confusion-zone collection of points is plotted.

plotted as a function of S_p for the four plasmas in four different colors. In the grouping of points to the left, the blue ejecta points are buried under the points of the other three plasma types. In the blue points to the right, in the figure, S_α of the ejecta is plotted as a function of $100S_p$ to shift the points two decades to the right where they can be viewed. As can be seen in Figure 15, there is a S_α versus S_p relationship holds for all four plasma types. This $S_p \leftrightarrow S_\alpha$ relation holding for all four types of plasma is indicated in Table 6. (This differs from the case in Figure 9 of the C^{6+}/C^{5+} versus O^{7+}/O^{6+} relations that differ in the different types of plasma.) Table 6 also indicates the state of the relations between S_α and O^{7+}/O^{6+} and C^{6+}/C^{5+}. The data in Figure 15 can be approximated with the relation $S_\alpha \approx 57 S_p^{1.1}$ (or, if the exponent of S_p is forced to be 1, $S_\alpha \approx 82 S_p$ is obtained). This fit is listed in the last column of Table 6, along with fits between S_α and O^{7+}/O^{6+} and between S_α and C^{6+}/C^{5+}.

In Figure 14 (fourth panel) the logarithm of the proton beta $\beta_p = 8\pi n_p k_B T_p / B^2$ from OMNI2 is binned for the four types of solar wind plasma. Ejecta (blue curve) have outstandingly low values of β_p compared with the other types of plasma [cf. *Gosling et al.*, 1987; *Lepping et al.*, 2005]. The highest values of β_p occur in the tail of the sector-reversal-region plasma distribution (purple): it is likely that these values might correspond to the high-β heliospheric plasma sheet [cf. *Winterhalter et al.*, 1994; *Crooker et al.*, 2004b].

In Figure 14 (fifth panel) the normalized amplitude $\delta B/B$ from OMNI2 of the magnetic field fluctuations in the solar wind is binned for the four categorizations of the solar wind. Here δB in the numerator is the amplitude of the vector magnetic field fluctuations, and B in the denominator is the average magnitude of B. In ejecta (blue curve), $\delta B/B$ is significantly less on average than the other three types of plasma. Statistically, $\delta B/B$ is largest in coronal-hole-origin plasma, but its mean value is only about 20% larger than the mean value in streamer-belt-origin plasma or in sector-reversal-region plasma (see Table 5).

3.3. Properties of Interest for the Earth

In Figure 16 the occurrence distributions of the Alfvén Mach number M_A, the ram (dynamic) pressure, the absolute value of the IMF latitude, and the Earth's *Kp* index (all from OMNI2) are plotted.

In Figure 16 (top) the Alfvén Mach number $M_A = v_{sw}/v_A$ of the solar wind at Earth is binned for the four types of solar wind plasma. The Alfvén Mach number is an important parameter for the driving of the Earth by the solar wind, with the nature of the Earth's reaction to the solar wind differing for low-Mach-number solar wind versus high-Mach-number solar wind [*Borovsky and Denton*, 2006; *Lavraud and Borovsky*, 2008; *Lopez*

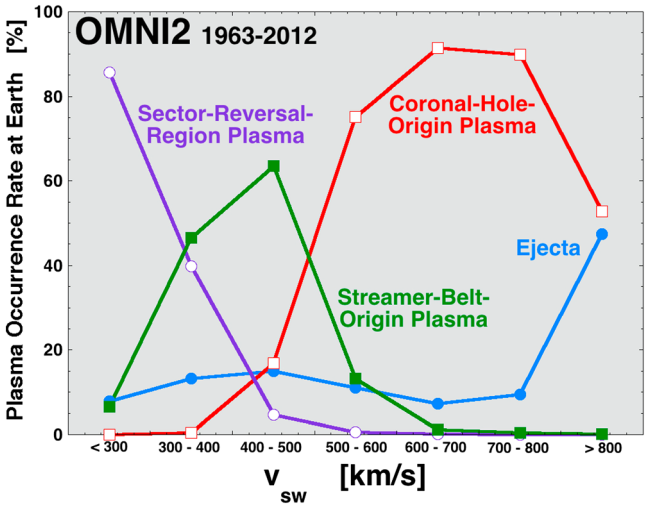

Figure 13. Separating the categorized OMNI2 data set into solar wind speed v_{sw} bins (labeled on the horizontal axis), the fraction of occurrence of each of the four types of solar wind plasma in each velocity bin is plotted (four colors).

et al., 2011]. At about $M_A = 6$ the plasma beta of the magnetosheath switches from a low-β flow at lower Mach numbers to a high-beta flow at higher Mach numbers [*Borovsky*, 2013]. As can be seen in Figure 16 (top), the M_A values for ejecta are nearly all under $M_A = 6$. (This low Mach number for magnetic clouds and ejecta has been noted in Figure 4 of *Borovsky and Denton* [2006].) Figure 16 indicates that the Alfvén Mach number of the solar wind is above 6 most of the time for the three nonejecta types of solar wind plasma. Note also the anomalously high Mach numbers for the sector-reversal-region plasma, even though the speed v_{sw} of that type of plasma is anomalously low (see Table 5 and Figure 13). Shocks with very high Alfvén Mach numbers have come into recent interest [cf. *Masters et al*., 2013; *Matsumoto et al*., 2013], so the Earth's bow shock during the passage of sector-reversal-region plasma may be of interest.

In Figure 16 (second panel) the dynamic pressure $P_{ram} = (1 + 4\alpha/p)\, n_p v_{sw}^2$ of the solar wind is binned for the four types of plasma. The ram pressure of the solar wind compresses the dayside magnetosphere [*Wing and Sibeck*, 1997] and large values of the ram pressure can lead to rapid loss of the outer electron radiation belt [*Onsager et al*., 2007; *Borovsky and Denton*, 2010c]. Note that the ram pressure is also the solar wind momentum flux density [*Lopez et al*., 1986; *Schwenn*, 2006]. On average all four types of plasma have similar values of P_{ram}; however, the lowest values occur for ejecta (blue curve) and the highest values occur for ejecta and for sector-reversal-region plasma (purple).

In Figure 16 (third panel) the occurrence distributions of the absolute value of the IMF latitude $|B_{lat}|$ (angle of the magnetic field vector out of the ecliptic plane) are plotted for the four plasma categorizations of the solar wind. These values are hourly averages in OMNI2. The number of occurrences (vertical) is plotted logarithmically so that the distribution of values that are highly out of the ecliptic ($|B_{lat}| > 60^o$) can be examined. For $|B_{lat}| > 60^o$, the occurrence rates in ejecta (blue) and in sector-reversal-region plasma (purple) are about twice as high as the occurrence rates in streamer-belt-origin plasma (green); for $|B_{lat}| > 60^o$, the occurrence rates in ejecta (blue) and in sector-reversal-region plasma (green) are about 4 times as high as the occurrence rates in coronal-hole-origin plasma (red). Strong driving of the Earth's magnetosphere is associated with intervals when the IMF is strongly (southward) out of the ecliptic plane [*Rostoker and Falthammar*, 1967; *Richardson*, 2013; *Zhang et al*., 2014]. For the origin of the solar wind, non-Parker-spiral intervals are also indicators of how the solar wind plasma was born; non-Parker-spiral intervals have been associated with ejecta [*Burlaga et al*., 1981; *Richardson and Cane*, 1996; *Smith and Phillips*, 1996] (cf. Figure 3 of *Borovsky* [2010]) and also with sector reversals and magnetic holes [*Borovsky*, 2010]. In comparing the plot of Figure 16 (third panel) with line 15 of Table 3, it must be remembered that line 15 of Table 3 applies to intervals that are sustained for 3 h and more and that Table 3 is the fraction of the data points within a given solar wind plasma type, whereas Figure 16 is the fraction of a given plasma that is the event.

In Figure 16 (fourth panel) the occurrence distributions of the *Kp* geomagnetic index of the Earth are plotted for the four types of solar wind plasma at Earth. *Kp* is a very good indicator of the strength of convection in the Earth's magnetosphere [*Thomsen*, 2004], which is a good indicator of the amount of coupling of the solar wind to the Earth. On average, *Kp* is higher when coronal-hole-origin plasma is passing the Earth than when the other three types of plasma are passing the Earth (cf. Table 5). Most likely this is because the velocity of the coronal-hole-origin plasma is higher on average than the velocities of the other three

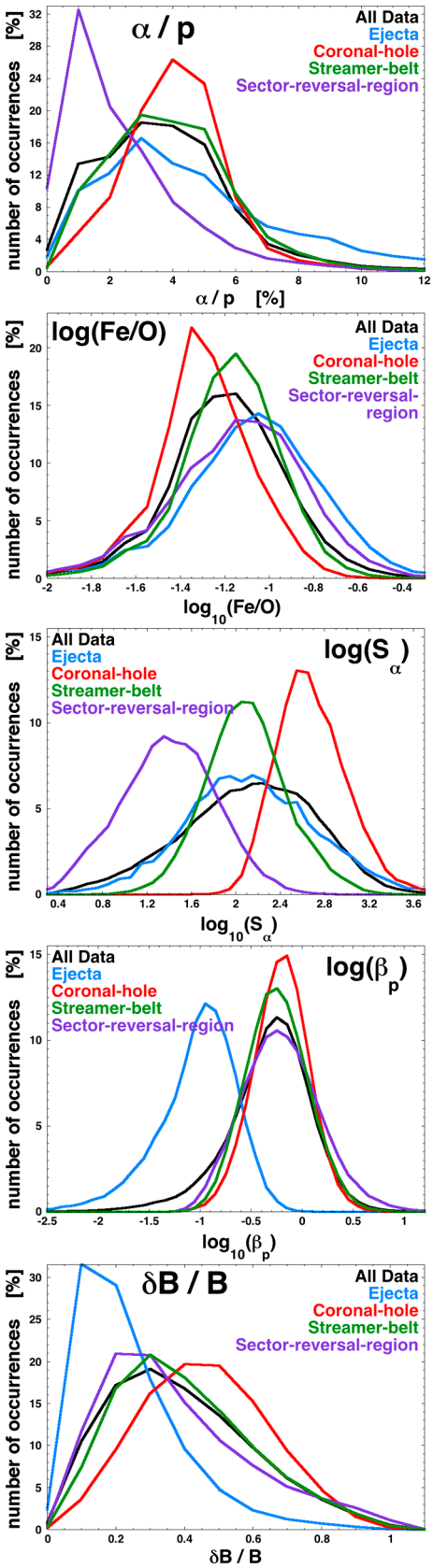

plasma types (see Figure 13), and it is well known that *Kp* has a positive correlation with solar wind velocity [e.g., *Snyder et al.*, 1963]. Note in Figure 16 (fourth panel) that the largest values of *Kp* (*Kp* > 7) are associated with ejecta; it is well known that the most severe geomagnetic storms are associated with coronal mass ejections [*Gosling*, 1993; *Richardson et al.*, 2001; *Zhang et al.*, 2007; *Echer et al.*, 2008].

4. The Occurrence Rates of the Four Types of Solar Wind Plasma

In Figure 17 the fraction of the time that the OMNI2 data set [*King and Papitashvili*, 2005] contains sufficient data to make a solar wind categorization is plotted as a function of time from 1963 to 2013. A 100 day (2400 h) running average is used. To make a categorization with the S_p, v_A, T_{exp}/T_p scheme of section 2.2, simultaneous measurements of the proton number density n_p, the proton temperature T_p, the magnetic field strength *B*, and the solar wind speed v_{sw} are needed. In the years 1995 onward (era of Wind and ACE), the data coverage at Earth is very good; prior to 1995 the data coverage is mixed, depending on the solar wind missions that were active at Earth. In the OMNI2 data set a total of 277,026 h are categorized.

In Figure 18 the results of categorizing the individual hours of the 1963–2013 OMNI2 data set are plotted. The bins are 100 days wide and the fractional categorizations of all of the available solar wind data in each 100 day interval are reported. The four colored bands represent the fraction of time in each 100 day band that each of the four plasmas occurs: the blue band is the fraction of time ejecta occurs, the red band is the fraction of time coronal-hole-origin plasma occurs, the green band is the fraction of time streamer-belt-origin plasma occurs, and the purple band is the fraction of time sector-reversal-region plasma occurs. The white curve across the top of the plot is 100 − SSN/5, where SSN is the international sunspot number. As can be seen, the fraction of time ejecta is passing the Earth (blue) is highly correlated with the sunspot number.

In Figure 19 the results of categorization of the solar wind with the three-parameter S_p-v_{sw}-T_{exp}/T_p scheme are compared with the results of categorization with the *Zhao et al.* [2009] O^{7+}/O^{6+}-v_{sw} scheme over the years when ACE O^{7+}/O^{6+} data is available. The blue curves are the fractions from the S_p-v_{sw}-T_{exp}/T_p scheme and the

Figure 14. For the four types of plasma, the distributions of values of five parameters are plotted. The parameters are (first panel) the alpha-to-proton density ratio α/p (from OMNI2), (second panel) $\log_{10}$ (Fe/O) (from ACE), (third panel) $\log_{10}$ (S_α) (from ACE), (fourth panel) $\log_{10}$ (β_p) (from ACE), and (fifth panel) $\delta B/B$ (from OMNI2).

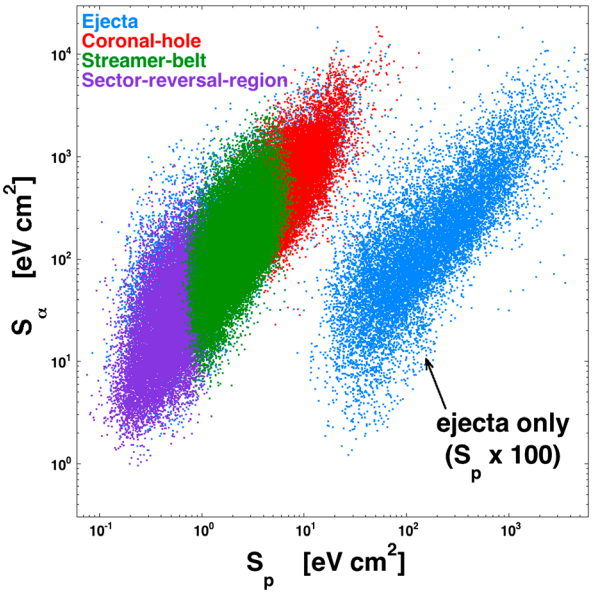

Figure 15. The alpha-particle-specific entropy S_α is plotted as a function of the proton-specific entropy S_p for the four types of solar wind plasma (four colors). The blue ejecta points underlying the other three colors at the left are replotted and shifted two decades to the right. The data are from ACE.

red curves are the fractions from the O^{7+}/O^{6+}-v_{sw} scheme. Figure 19 (top) is the fraction of time ejecta is found in the two categorization schemes: for all years that the S_p-v_{sw}-T_{exp}/T_p scheme identifies more ejecta in the solar wind than does the O^{7+}/O^{6+}-v_{sw} scheme. Figure 19 (middle) plots the fraction of coronal-hole-origin plasma found in the two schemes; the two-parameter O^{7+}/O^{6+}-v_{sw} scheme (red) assigns more plasma to the coronal hole category than does the three-parameter S_p-v_{sw}-T_{exp}/T_p scheme (blue). Note in the solar minimum years 2008 and 2009 the O^{7+}/O^{6+}-v_{sw} scheme assigns almost 100% of the wind to the coronal hole category (see also Figure 1 of *Zhao et al.* [2009]); this is in contrast to the standard knowledge that the solar wind at Earth during solar minimum is an alternating mix of coronal hole and streamer belt plasma [cf. *Bame et al.*, 1976; *Richardson et al.*, 2000; *Richardson and Cane*, 2012] with sector reversals, which cannot be in coronal hole plasma. In Figure 19 (middle) the S_p-v_{sw}-T_{exp}/T_p scheme (blue) finds a mix of plasma during those solar minima years. Figure 19 (bottom) plots the fraction of "noncoronal hole plasma" found by the O^{7+}/O^{6+}-v_{sw} scheme and the amount of "total streamer-belt-origin plasma" (the sum of the streamer-belt-origin plasma and sector-reversal-region plasma) found by the S_p-v_{sw}-T_{exp}/T_p scheme. In the solar-minimum years (e.g., 2008–2009) the three-parameter S_p-v_{sw}-T_{exp}/T_p scheme (blue) identifies much more streamer belt plasma than does the O^{7+}/O^{6+}-v_{sw} scheme (red). Recall that the two schemes are compared with known collections of solar wind plasmas in Table 1.

Concerning the identification by the O^{7+}/O^{6+}-v_{sw} scheme of the solar-minimum solar wind as ~100% coronal hole plasma (Figure 1 of *Zhao et al.* [2009]), systematic changes in the O^{7+}/O^{6+} ratio as a function of v_{sw} through the solar cycle have been identified [cf. *Schwadron et al.*, 2011; *Kasper et al.*, 2012]. (See also the warning by *Lepri et al.* [2013] about using heavy-ion charge-state ratios to categorize the solar wind.) Perhaps if those solar cycle variations in O^{7+}/O^{6+} were to be incorporated into a *Zhao et al.* [2009] type of scheme, the solar minimum problems of the scheme could be reduced.

In Figure 18 a clear correlation between the fraction of ejecta occurring and the sunspot cycle was seen. In Figure 20 the fractional rate of occurrence of ejecta (blue) and sector-reversal-region plasma (purple) are plotted as a function of the sunspot number SSN. Each plotted point is obtained from 100 days of data (from Figure 18). Least squares linear regression fits are made to the ejecta points (blue) and the sector-reversal-region plasma points (purple). The Pearson linear correlation coefficient r_{corr} [*Bevington and Robinson*, 1992, equation (11.17)] between the occurrence fraction and SSN appears on the figure for ejecta and sector-reversal-region plasma. Each plasma has $N = 66$ data points for the correlation-coefficient calculation; uncorrelated data would have correlation coefficients r_{corr} in the range of $\pm 2/N^{1/2}$ [e.g., *Beyer*, 1966; *Bendat and Piersol*, 1971], which is $r_{corr} \sim \pm 0.25$ for $N = 66$. Accordingly, the occurrence fractions of streamer-belt-origin plasma ($r_{corr} = -0.03$) and coronal-hole-origin plasma ($r_{corr} = -0.16$) are uncorrelated with SSN. The correlation coefficient ($r_{corr} = 0.84$) between the occurrence fraction of ejecta (blue) and SSN is quite high on Figure 20, indicating a high correlation between the two values. The linear regression fit between the occurrence fraction of ejecta F_e (in %) and the sunspot number SSN is

$$F_e = 3.1 + 0.16\ \mathrm{SSN}. \tag{11}$$

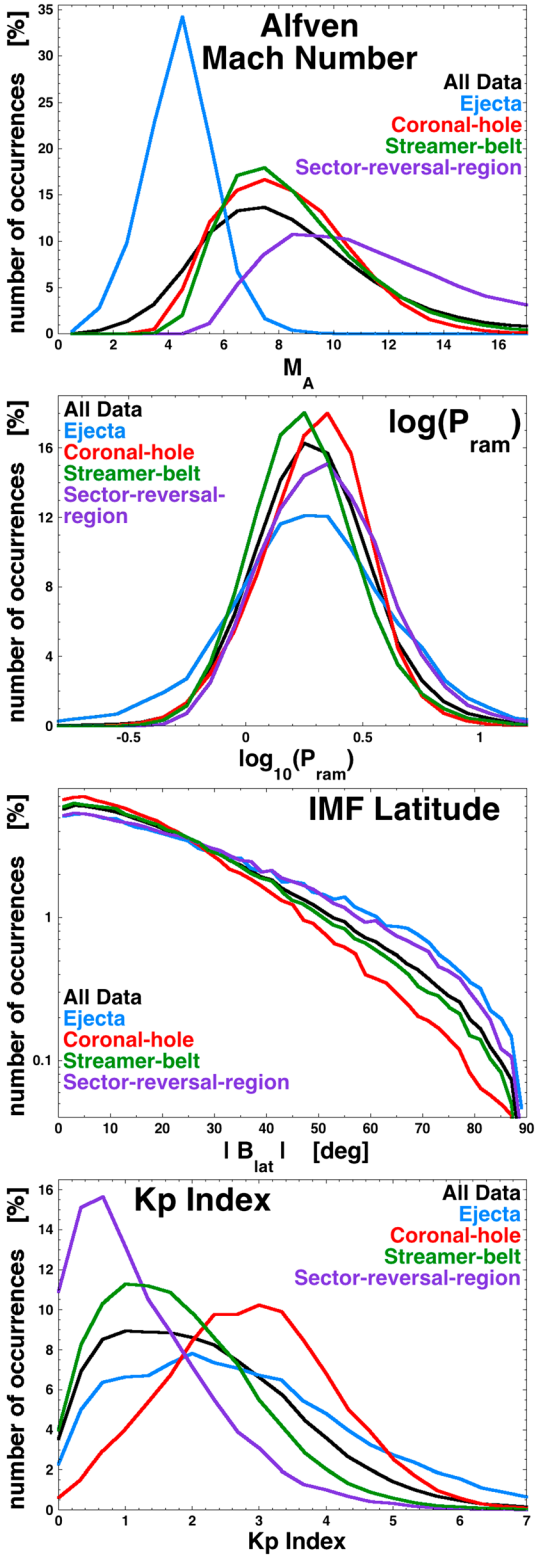

The occurrence fraction of sector-reversal-region plasma with (with $r_{corr} = -0.49$) shows a definite anticorrelation with SSN.

In Figure 21 the 1963–2013 data on the occurrences at Earth of the four types of solar wind plasma are binned into the four phases of the solar cycle for the more than four solar cycles spanned by the OMIN2 data set. The onsets of the phases of the solar cycle were determined by eye from a temporal plot of the sunspot number. When the sunspot number began to increase strongly away from solar minimum, the onset of the ascending phase was declared; when the temporal increase of the sunspot number began to become slow, the onset of solar maximum was declared; when the temporal decrease of the sunspot number became strong, the onset of the declining phase was declared; and when the temporal decrease of the sunspot number became weak, the onset of solar minimum was declared. The strong trend in the occurrence fraction of ejecta (blue curve) is clearly seen, with a minimum in the occurrence of ejecta during solar minimum and a maximum in the occurrence of ejecta at solar maximum, as is well known [e.g., *Gopalswamy*, 2006; *Richardson and Cane*, 2010]. During solar minimum when ejecta are more rare, the solar wind at Earth is known to be an alternating mix of coronal hole and streamer belt plasma [cf. *Bame et al.*, 1976; *Richardson et al.*, 2000]; Figure 21 points out further that it is a mix of coronal-hole-origin plasma, streamer-belt-origin plasma, and sector-reversal-region plasma. The occurrence rate of the sector-reversal-region plasma shows a peak at solar minimum (this will be explored further in Figure 22). The occurrence fraction of coronal-hole-origin plasma (red curve) shows a peak during the declining phase of the solar cycle; it is well known that long-duration repeating high-speed streams are prevalent during the declining phase [cf. *Bame et al.*, 1976; *Xystouris et al.*, 2014] giving rise to 27 day repeating intervals of high geomagnetic activity [*Richardson et al.*, 2000; *Borovsky and Denton*, 2006]. This trend in the occurrence rate of coronal-hole-origin plasma would not show up in an occurrence versus SSN plot (such as Figure 20) since declining phases and

Figure 16. For the four types of plasma, the distributions of values of four solar wind parameters that affect the Earth are plotted. The parameters are the (top panel) Alfvén Mach number M_A (from OMNI2), (second panel) $\log_{10}$ (P_{ram}) (from ACE), (third panel) the absolute value of the IMF latitude B_{lat} (from ACE), and (fourth panel) the value of the Earth's *Kp* index (from OMNI2).

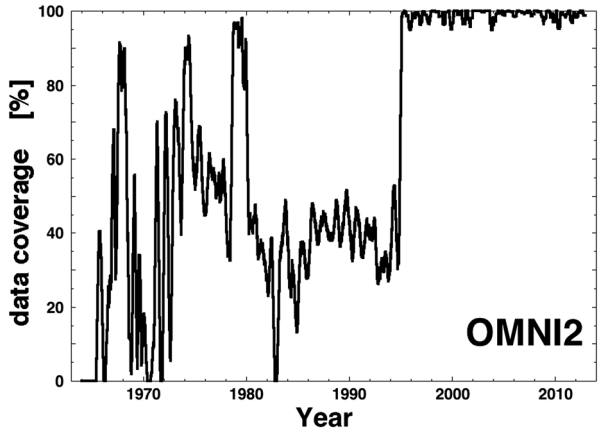

Figure 17. The fraction of data coverage (simultaneous values of n_p, T_p, B, and v_{sw}) in the OMNI2 1 h data set from 1963 to 2014 is plotted as a function of year. The black curve is a 100 day wide running average.

ascending phases have approximately the same values of SSN. Streamer-belt-origin plasma (green curve in Figure 21) dominates the occurrence fraction throughout the solar cycle; if "total streamer-belt-origin" plasma were considered (summing the streamer-belt-origin plasma and the sector-reversal-region plasma together), then total streamer-belt-origin plasma would clearly dominate all phases of the solar cycle.

Solar cycle dependence of the newer category of plasma, the sector-reversal-region plasma, is explored further in Figure 22. The four-plasma occurrences are binned into 300 day wide (7200 h wide) intervals for the OMNI2 data set and the fraction of occurrence of sector-reversal-region plasma to total streamer-belt plasma (streamer-belt-origin plasma plus sector-reversal-region plasma) is calculated for every 300 day bin and the fraction is plotted in blue in Figure 22. Only 300 day bins that had data coverage of 25% of the time or more (cf. Figure 17) are used in the plot. The sunspot number divided by 10 is plotted in red to gauge the phase of the solar cycle. Examining the blue and red curves in Figure 22, the fraction of the total-streamer-belt-origin plasma that is sector-reversal-region plasma is maximum at solar minimum and the fraction that is sector-reversal-region plasma is minimum at solar maximum. This could mean that the fraction of streamers that are pseudostreamers (without sector-reversal-region plasma) is higher during solar maximum. Or, (a) since ejecta is maximizing during solar maximum and (b) since some ejecta comes from helmet streamers [*Wang et al.*, 2000; *Foullon et al.*, 2011], it could mean that quiescent helmet streamers are more rare during solar maximum. A reviewer has suggested that a reason that Figure 22 shows a high occurrence rate of sector-reversal-region plasma at solar minima is that spacecraft in the ecliptic plane spend much time skimming the heliospheric current sheet near solar minima.

5. Summary

The development of the categorization scheme and the findings made using that scheme are summarized in the five subsections that follow.

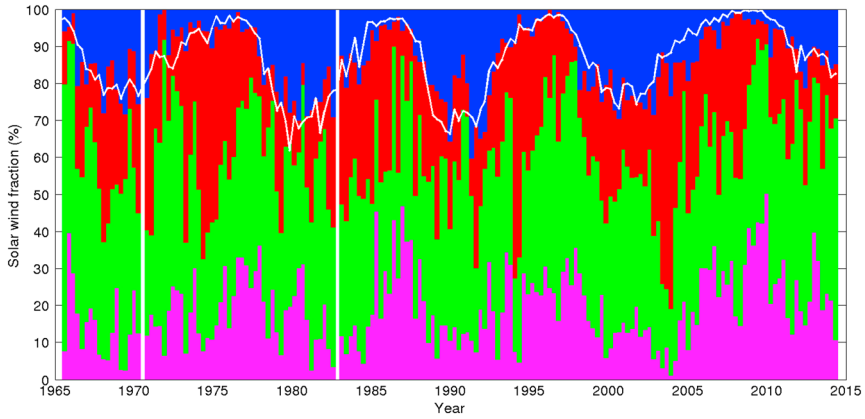

Figure 18. A categorization of the OMNI2 data set by the three-parameter S_p-v_{sw}-T_{exp}/T_p scheme is used to produce an overview of four kinds of plasma occurrence rates of the four types of plasma at Earth over four solar cycles. The four plasmas are ejecta (blue), coronal-hole-origin plasma (red), streamer-belt-origin plasma (green), and sector-reversal-region plasma (purple). The white curve is 100 − 0.2 SSN and the white vertical bands represent intervals with insufficient solar wind data.

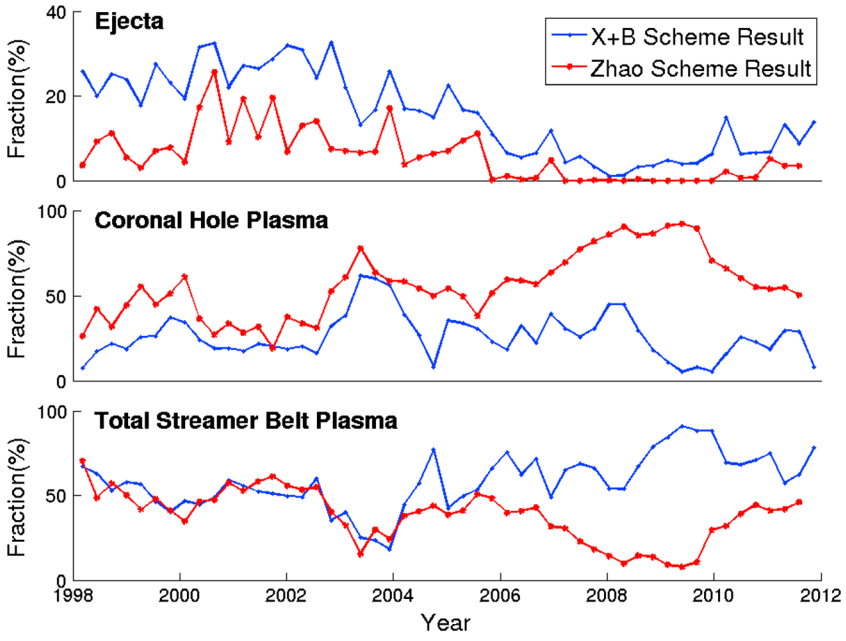

Figure 19. (top, middle, and bottom) The occurrence fractions for three types of plasma are compared for the S_p-v_{sw}-T_{exp}/T_p scheme developed here (blue) and for the O^{7+}/O^{6+}-v_{sw} scheme of *Zhao et al.* [2009] (red). "Total streamer belt plasma" is streamer-belt-origin plasma plus sector-reversal-region plasma.

5.1. The Categorization Scheme

An algebraic scheme was developed to categorize the solar wind plasma into four types: coronal-hole-origin plasma, streamer-belt-origin plasma, sector-reversal-region plasma, and ejecta. The scheme uses three solar wind parameters: (1) the proton-specific entropy $S_p = T_p/n_p^{2/3}$, (2) the proton Alfvén speed $v_A = B/(4\pi m_p n_p)^{1/2}$, and (3) the ratio of the measured proton temperature T_p compared with the velocity-dependent expected temperature for the solar wind speed $T_{exp} = (v_{sw}/258)^{3.113}$. To evaluate those three parameters, measurements are needed of four solar wind quantities: the proton number density n_p, the proton temperature T_p, the magnetic field strength B, and the solar wind speed v_{sw}.

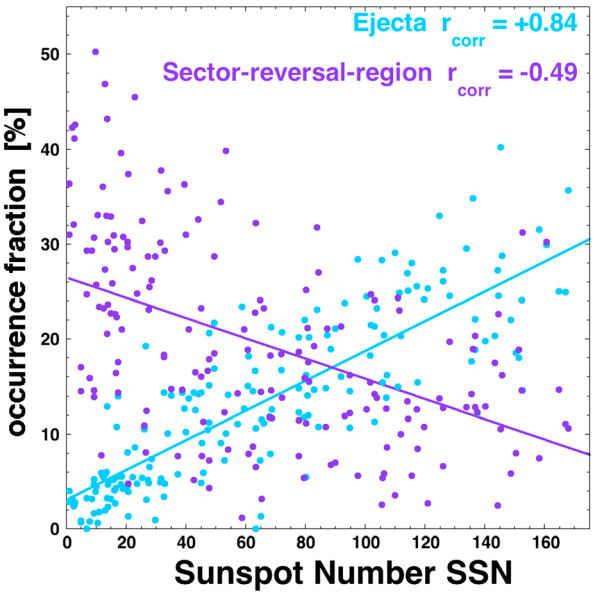

Figure 20. For ejecta (blue) and sector-reversal-region plasma (purple), the occurrence fraction is plotted as a function of the sunspot number. Each plotted point is for a 100 day interval. The Pearson linear correlation coefficients for all four types of plasma are indicated on the plot.

The three-parameter categorization scheme is versatile in that (1) it does not require measurements of the heavy-ion charge states of the solar wind and (2) it does not require looking at the time history of the solar wind nor at the recent occurrences of solar wind events.

The categorization scheme was developed by using collections of solar wind plasma of known types, such as (a) unperturbed coronal hole plasma from constant velocity high-speed streams, (b) published magnetic clouds, and (c) collected pseudostreamers.

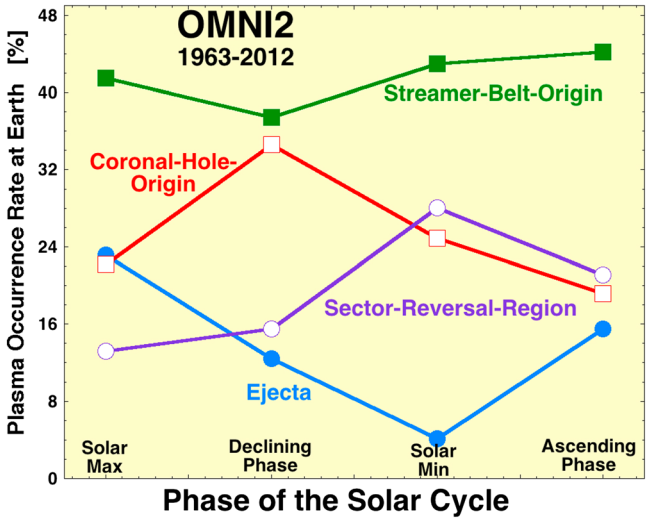

Figure 21. The 1963–2013 OMNI2 data set is divided into the four phases of the solar cycle, and the fraction of each phase, that is, ejecta is plotted in blue, sector-reversal-region plasma is plotted in purple, coronal-hole-origin plasma is plotted in red, and streamer-belt-origin plasma is plotted in green.

The scheme was assessed against those known collections of plasma and found to be very satisfactory. The scheme was tested against an existing two-parameter scheme and found to be an improvement.

The common categorization of the solar wind into fast wind and slow wind was compared with the categorization by the three-parameter scheme. Ejecta contamination is always a problem for fast wind/slow wind categorization. A selection of "fast wind" is found to result in a collection of mostly coronal-hole-origin plasma (with ejecta): a selection of "slow wind" is found to result in a mix of streamer-belt-origin plasma, sector-reversal-region plasma, and coronal-hole-origin plasma (with ejecta).

5.2. The Fourth Plasma Type: Sector-Reversal-Region Plasma

The usual streamer-belt-plasma category was split into two categories: streamer-belt-origin plasma and sector-reversal-region plasma. The candidate population for sector-reversal-region plasma was identified only by the properties of the electron strahl around sector reversals. The values of S_p, v_A, and T_{exp}/T_p for that candidate population were then used to define a region in S_p-v_A-T_{exp}/T_p parameter space that would be categorized as sector-reversal-region plasma. Examining the data points in OMNI2 that are categorized as sector-reversal-region plasma by their S_p-v_A-T_{exp}/T_p values, it is found that those regions indeed reside around magnetic sector reversals.

A statistical examination of the solar wind that is categorized as sector-reversal-region plasma finds that sector-reversal-region plasma has very low values of the α/p density ratio and sector-reversal-region plasma is likely to be the cores of helmet streamers: such plasma types were suggested by *Bavassano et al.* [1997] (stalks of coronal streamers) and by *Wang et al.* [2000] (dynamic streamers). Sector-reversal-region plasma has anomalously high Alfvén Mach numbers and the *Kp* index of the Earth is typically quite low when sector-reversal-region plasma is passing. The relationship between C^{6+}/C^{5+} and O^{7+}/O^{6+} for sector-reversal-region plasmas resembles that of magnetic clouds.

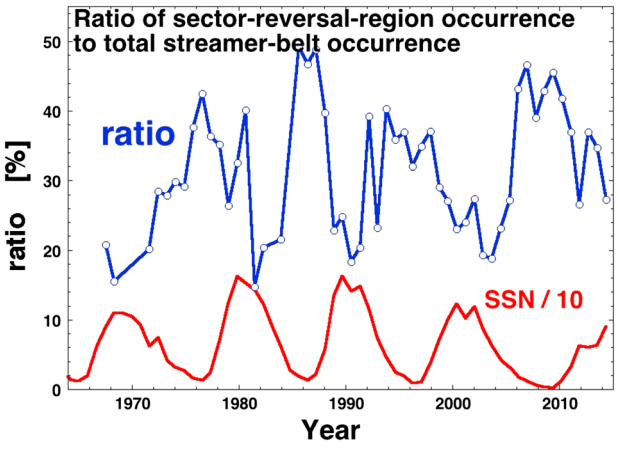

Figure 22. Defining "total streamer belt plasma" to the streamer-belt-origin plasma plus sector-reversal-region plasma, the ratio of the amount of sector-reversal-region plasma to the amount of total streamer belt plasma that occur in 300 day wide interval is plotted as a function of time for the OMNI2 data set.

The fraction of the total streamer belt plasma that is sector-reversal-region plasma is maximum at solar minimum and minimum at solar maximum. Some suggested reasons why this might be so are given in the manuscript.

5.3. Properties of the Plasma Types

The statistical properties of the categorized plasmas were examined. Ejecta was found to have low values of the Alfvén Mach number *MA*, low values of the proton beta β_p, and low values of the normalized

amplitude of the magnetic field fluctuations $\delta B/B$. The amplitude $\delta B/B$ was largest on average in coronal-hole-origin plasma, but it was only tens of per cent larger than in streamer-belt-origin plasma and sector-reversal-region plasma. Sector-reversal-region plasma has very low values of α/p and high Alfvén Mach numbers. The large deviations of the solar wind magnetic field direction out of the ecliptic plane occur predominantly in ejecta and sector-reversal-region plasma.

5.4. Relations Between S_p, S_α, O^{7+}/O^{6+}, and C^{6+}/C^{5+}

The correlations between the four parameters S_p, S_α, O^{7+}/O^{6+}, and C^{6+}/C^{5+} were examined for the four types of solar wind plasma. Six mathematical relations between the four parameters are found: each of these mathematical relations holds for some of the four plasmas. The $S_\alpha \leftrightarrow S_p$ formula holds for all four types of plasma. The $O^{7+}/O^{6+} \leftrightarrow S_p$ and $O^{7+}/O^{6+} \leftrightarrow S_\alpha$ formulas hold for coronal-hole-origin plasma, streamer-belt-origin plasma, and sector-reversal-region plasma; they do not hold for ejecta. The $C^{6+}/C^{5+} \leftrightarrow S_p$, the $C^{6+}/C^{5+} \leftrightarrow S_\alpha$, and the $C^{6+}/C^{5+} \leftrightarrow O^{7+}/O^{6+}$ formulas hold for coronal-hole-origin plasma and streamer-belt-origin plasma; they do not hold for ejecta or for sector-reversal-region plasma. In plots of C^{6+}/C^{5+} versus O^{7+}/O^{6+}, points that are categorized as ejecta fall into two populations, one population that tracks the C^{6+}/C^{5+} versus O^{7+}/O^{6+} relationship of streamer belt plasma and coronal hole plasma and one population that tracks the C^{6+}/C^{5+} versus O^{7+}/O^{6+} pattern of magnetic clouds and sector reversal regions. From these $C^{6+}/C^{5+} \leftrightarrow O^{7+}/O^{6+}$ relations, it is speculated (1) that the birth mechanisms of coronal-hole-origin plasma and of streamer-belt-origin plasma may be very similar to each other and (2) that the birth mechanisms of magnetic-cloud-type ejecta and of sector-reversal-region plasma may be very similar to each other.

5.5. Occurrence Rates at Earth

The well-known relations (1) that ejecta occurs most prevalently at solar maximum and rarely at solar minimum and (2) that coronal-hole-origin plasma occurs most prevalently during the declining phase and less prevalently during the ascending phase were both seen.

A strong correlation between the occurrence rate of ejecta and the sunspot number is seen. A modest anticorrelation between the sunspot number and the occurrence rate of sector-reversal-region plasma is seen.

The three-parameter categorization scheme finds solar minimum to be a mix of streamer-belt-origin plasma, sector-reversal-region plasma, and coronal-hole-origin plasma; this is contrary to an earlier categorization scheme which has coronal-hole-origin plasma dominating at solar minimum.

6. Discussion and Future Studies

No plasma categorization scheme will be exact, owing to our lack of knowledge about the exact origins of solar wind from the Sun and our incomplete understanding of how the plasma origin is manifested as signatures in the solar wind. However, the three-parameter categorization scheme developed in this report is quite accurate when used to categorize known intervals of solar wind plasma, such as (a) unperturbed coronal hole plasma from constant velocity high-speed streams, (b) published magnetic clouds, and (c) collected pseudostreamers.

In this report a fourth solar wind plasma category has been defined: sector-reversal-region plasma. This is in addition to the three standard categories of solar wind plasma: ejecta, coronal-hole-origin plasma, and streamer-belt-origin plasma. The parent population of the sector-reversal-region plasma is the "strahl confusion zones" around magnetic sector reversals. The sector-reversal-region plasma appears to be a definite, different type of plasma from the other three types. It is found to have low alpha-to-proton density ratios and higher-than-average Alfvén Mach numbers. It has statistical relations between C^{6+}/C^{5+} and S_p and between C^{6+}/C^{5+} and O^{7+}/O^{6+} that differ from the relations in coronal-hole-origin plasma and streamer-belt-origin plasma, more like the relations in magnetic clouds. This could be indicative of a birth mechanism for sector-reversal-region plasma that is related to the birth mechanism of magnetic-cloud-type ejecta. Future analysis of this sector-reversal-region plasma (such as a analysis of spectral indices, Alfvénicity, magnetic structure, and discontinuities) will be interesting.

This analysis also indicates that there are two populations of ejecta plasmas: a population with magnetic-cloud-like patterns of C^{6+}/C^{5+} versus O^{7+}/O^{6+} and a population with coronal-hole-like and streamer-belt-like patterns of C^{6+}/C^{5+} versus O^{7+}/O^{6+}. A future investigation of these two ejecta populations is called for.

For future research there are numerous solar wind studies that can be clarified by separating the solar wind data into the four different types of plasma. We have a rudimentary knowledge about the differences in the properties of turbulence (spectral slopes, Alfvénicities, and correlation lengths) in different types of solar wind plasma; this knowledge could be greatly improved by regularly separating solar wind data into the different plasma categories and separating the turbulence studies into those plasma categories. Similarly, our knowledge of the current sheets and pressure-balanced structures in the solar wind could be improved by separating studies into the appropriate types of solar wind plasma. The origin of several types of solar wind structures such as magnetic holes, ortho-Parker-spiral intervals, and nonecliptic magnetic field intervals are not known; information about these may be gained by statistically studying these intervals versus the types of plasma in which they occur.

Particle distribution functions and strahl properties also could be better organized versus the types of plasmas in which the observations are made. This is particularly true for the solar wind core halo electron distributions, where very little information exists as functions of the type of plasma.

To sort out systematic differences in the properties of the turbulence around shocks, interplanetary-shock data analysis needs to be sorted according to the type of plasma through which the shock propagates.

Connecting (a) the categorization of the plasma at 1 AU into four types with (b) model-based outward mappings of the solar wind from solar magnetograms to the Earth [e.g., *Arge et al*., 2004; *Owens et al*., 2005] would provide information about what types of regions on the Sun give rise to the four types of plasma and would conversely provide feedback to the mapping techniques about the origin of solar wind types at the Sun.

A more-detailed study of the occurrence rates of the four plasmas and the properties of the four plasmas may help to answer questions such as [*Georgieva et al*., 2006, 2012, 2013]: Are all solar cycles the same? Have there been long-term variations in the occurrence rates of solar wind plasmas reaching the Earth? Does this give rise to long-term variations in the magnetosphere-ionosphere-atmosphere system?

Studying the manner in which the solar wind drives the Earth's magnetosphere separately for the four types of solar wind plasma may shed light on whether or not reported differences in the driving of the Earth during the different phases of the solar cycle are simply caused by different mixes in the occurrence fractions of the four types of plasma during the different solar cycle phases.

Finally, a needed task for the future is a generalization of this three-parameter four-plasma categorization scheme for use closer to the Sun than 1 AU. Understanding existing and future $r < 1$ AU data sets is critical to gaining an understanding of the origins and evolutions of solar wind features that reach the Earth.

Appendix A: Vector-Product Method of Categorization

In point-normal format, the equations for the three planes (light blue, dark blue, and magenta, respectively) in Figure 6 are

$$5.92\left[\log_{10}(S_p) - 1.1\right] + 4\left[\log_{10}(v_A) - 2.5\right] + 3.108\left[\log_{10}(T_{exp}/T_p) + 2\right] = 0 \quad \text{(A1a)}$$

$$6.08\left[\log_{10}(S_p) + 0.3\right] + 4\left[\log_{10}(v_A) - 2.41\right] + 0.76\left[\left(\log_{10}(T_{exp}/T_p) + 2\right]\right. = 0 \quad \text{(A1b)}$$

$$-3.88\left[\log_{10}(S_p) + 1.5\right] + 14\left[\log_{10}(v_A) - 1.52\right] - 0.77\left[\log_{10}(T_{exp}/T_p) - 2\right] = 0 \quad \text{(A1c)}$$

Calling the light blue plane 1, the dark blue plane 2, and the magenta plane 3 (see Figure 6), a point p in each of the three planes (in $\log_{10}(S_p)$, $\log_{10}(v_A)$, $\log_{10}(T_{exp}/T_p)$ space) is (from expressions (A1a)–(A1c))

$$p_1 = (1.1\ ,\ 2.5\ , -2) \quad \text{(A2a)}$$

$$p_2 = (-0.3\ ,\ 2.41\ , -2) \quad \text{(A2b)}$$

$$p_3 = (-1.5\ ,\ 1.52\ ,\ 2) \quad \text{(A2c)}$$

The normal vectors (vectors underlined) of the three planes (in $\log_{10}(S_p)$, $\log_{10}(v_A)$, $\log_{10}(T_{exp}/T_p)$ space) are (from expressions (A1a)–(A1c))

$$\underline{n}_1 = (5.92\ ,\ 4.0\ ,\ 3.108) \quad \text{(A3a)}$$

$$\underline{n}_2 = (6.08\ ,\ 4.0\ ,\ 0.76) \quad \text{(A3b)}$$

$$\underline{n}_3 = (-3.88\ ,\ 14.0\ , -0.77). \quad \text{(A3c)}$$

Table A1. Vector-Scheme Categorization Rules for the Four Types of Solar Wind Plasma[a]

No.	Sign of g_3	Sign of g_2	Sign of g_1	Solar Wind Plasma Type
1	+			Ejecta
2	−		+	Coronal-Hole-Origin Plasma
3	−	−		Sector-Reversal-Region Plasma
4	−	+	−	Streamer-Belt-Origin Plasma

[a]If a cell is blank, the answer in that cell is irrelevant.

These three normals are shown as the red arrows in Figure 6. In $\log_{10}(S_p)$, $\log_{10}(v_A)$, $\log_{10}(T_{exp}/T_p)$ space, a data point can be specified as $d_x = \log_{10}(S_p)$, $d_y = \log_{10}(v_A)$, and $d_z = \log_{10}(T_{exp}/T_p)$. For the three planes, each data point can be used to construct three data vectors $\underline{\mathbf{d_1}}$, $\underline{\mathbf{d_2}}$, and $\underline{\mathbf{d_3}}$ going from the three points p_1, p_2, and p_3 to the data point (d_x, d_y, and d_z). Using expressions (A1a)–(A1c) for the coordinates of these three points on the planes, the three data vectors for each data point (d_x, d_y, and d_z) are

$$\underline{\mathrm{d}}_1 = \left(d_x - 5.92\ ,\ d_y - 4.0\ ,\ d_z - 3.108\right) \tag{A4a}$$

$$\underline{\mathrm{d}}_2 = \left(d_x - 6.08\ ,\ d_y - 4.0\ ,\ d_z - 0.76\right) \tag{A4b}$$

$$\underline{\mathrm{d}}_3 = \left(d_x + 3.88\ ,\ d_y - 14.0\ ,\ d_z + 0.77\right). \tag{A4c}$$

Three vector products (dot products) g_1, g_2, and g_3 are formed by the three data vectors $\underline{\mathbf{d_1}}$, $\underline{\mathbf{d_2}}$, and $\underline{\mathbf{d_3}}$ dotted into the respective normal vectors $\underline{\mathbf{n_1}}$, $\underline{\mathbf{n_2}}$, and $\underline{\mathbf{n_3}}$ to the three planes

$$g_1 = \underline{\mathrm{d}}_1 \cdot \underline{\mathrm{n}}_1 \tag{A5a}$$

$$g_2 = \underline{\mathrm{d}}_2 \cdot \underline{\mathrm{n}}_2 \tag{A5b}$$

$$g_3 = \underline{\mathrm{d}}_3 \cdot \underline{\mathrm{n}}_3 \tag{A5c}$$

where $\underline{\mathbf{d}}$ and $\underline{\mathbf{n}}$ are given by expressions (A4a)–(A4c) and (A3a–A3c). The sign of the three vector products g_1, g_2, and g_3 are the inputs to the algorithm to categorize the data point. This algorithm is laid out in Table A1; A blank cell in the table means "any value is acceptable."

One advantage to this vector method of categorization is that the vector product of two arrays can be performed in one operation, i.e., a data set can be categorized in one vector operation on a computer.

Acknowledgments
The authors thank Mick Denton, Gang Li, Ruth Skoug, John Steinberg, and Michelle Thomsen for helpful conversations. F.X. wishes to thank the Los Alamos National Laboratory for a Vela Fellowship while attending the Los Alamos Space Weather Summer School. This work was supported at the Space Science Institute by the NSF Solar-Terrestrial Program, the NASA Magnetospheric Guest Investigators program, and the NASA Heliophysics LWS Program; at the University of Michigan by the NASA Geospace SR&T Program; and at Lancaster University by Science and Technology Funding Council grant ST/I000801/1. The hourly averaged OMNI2 measurements and the ACE measurements used in this paper are available from NASA data server websites (http://omniweb.gsfc.nasa.gov/form/dx1.html and http://cdaweb.gsfc.nasa.gov/istp_public/).

Yuming Wang thanks Ian G. Richardson and Nancy Crooker for their assistance in evaluating this paper.

References

Aellig, M. R., S. Hefi, H. Gunwaldt, P. Bochsler, P. Wurz, F. M. Ipavich, and D. Havestadt (1999a), The Fe/O elemental abundance ratio in the solar wind, *J. Geophys. Res.*, *104*, 2479.

Aellig, M. R., H. Holweger, P. Bochsler, P. Wurz, H. Grunwaldt, S. Hefti, F. M. Ipavich, and B. Klecker (1999b), The Fe/O elemental abundance ratio in the solar wind, *AIP Conf. Proc.*, *471*, 255.

Antiochos, S. K., Z. Mikic, V. S. Titov, R. Lionello, and J. A. Linker (2011), A model for the sources of the slow solar wind, *Astrophys. J.*, *731*, 112.

Antonucci, E., L. Abbo, and M. A. Dodero (2005), Slow wind and magnetic topology in the solar minimum corona in 1996–1997, *Astron. Astrophys.*, *435*, 699.

Arge, C. N., D. Odstrcil, V. J. Pizzo, and L. R. Mayer (2003), Improved method for specifying solar wind speed near the Sun, *AIP Conf. Proc.*, *679*, 190.

Arge, C. N., J. G. Luhmann, D. Odstrcil, C. J. Schrijver, and Y. Li (2004), Stream structure and coronal sources of the solar wind during the May 12th, 1997 CME, *J. Atmos. Sol. Terr. Phys.*, *66*, 1295–1309.

Arya, S., and J. W. Freeman (1991), Estimates of solar wind velocity gradients between 0.3 and 1 AU based on velocity probability distributions from Helios 1 at perihelion and aphelion, *J. Geophys. Res.*, *96*, 14,183–14,187.

Asbridge, J. R., S. J. Bame, W. C. Feldman, and M. D. Montgomery (1976), Helium and hydrogen velocity differences in the solar wind, *J. Geophys. Res.*, *81*, 2719–2727.

Bame, S. J., J. R. Asbridge, W. C. Feldman, and J. T. Gosling (1976), Solar cycle evolution of high-speed solar wind streams, *Astrophys. J.*, *207*, 977–980.

Bame, S. J., J. R. Asbridge, W. C. Feldman, and J. T. Gosling (1977), Evidence for a structure-free state at high solar wind speeds, *J. Geophys. Res.*, *82*, 1487–1492.

Bavassano, B., R. Woo, and R. Bruno (1997), Heliospheric plasma sheet and coronal streamers, *Geophys. Res. Lett.*, *24*, 1655–1685.

Bendat, J. S., and A. G. Piersol (1971), *Random Data: Analysis and Measurement Procedures*, Sect. 4.8.1, John Wiley, New York.

Bevington, P. R., and D. K. Robinson (1992), *Data Reduction and Error Analysis for the Physical Sciences*, 2nd ed., McGraw-Hill, New York.

Beyer, W. H. (Ed.) (1966), *Handbook of Tables for Probability and Statistics*, Sect. IX, Chem. Rubber, Cleveland, Ohio.

Blanco, J. J., J. Rodriquez-Pacheco, M. A. Hidalgo, and J. Sequeiros (2006), Analysis of the heliospheric current sheet fine structure: Single or multiple currents sheets, *J. Atmos. Sol. Terr. Phys.*, *68*, 2173.

Borovsky, J. E. (2008), The flux-tube texture of the solar wind: Strands of the magnetic carpet at 1 AU?, *J. Geophys. Res.*, *113*, A08110, doi:10.1029/2007JA012684.
Borovsky, J. E. (2010), On the variations of the solar-wind magnetic field about the Parker-spiral direction, *J. Geophys. Res.*, *115*, A09101, doi:10.1029/2009JA015040.
Borovsky, J. E. (2012a), The velocity and magnetic-field fluctuations of the solar wind at 1 AU: Statistical analysis of Fourier spectra and correlations with plasma properties, *J. Geophys. Res.*, *117*, A05104, doi:10.1029/2011JA017499.
Borovsky, J. E. (2012b), The effect of sudden wind shear on the Earth's magnetosphere: Statistics of wind-shear events and CCMC simulations of magnetotail disconnections, *J. Geophys. Res.*, *117*, A06224, doi:10.1029/2012JA017623.
Borovsky, J. E. (2012c), Looking for evidence of mixing in the solar wind from 0.31 to 0.98 AU, *J. Geophys. Res.*, *117*, A06107, doi:10.1029/2012JA017525.
Borovsky, J. E. (2013), Physics based solar-wind driver functions for the magnetosphere: Combining the reconnection-coupled MHD generator with the viscous interaction, *J. Geophys. Res. Space Physics*, *118*, 7119–7150, doi:10.1002/jgra.50557.
Borovsky, J. E., and M. H. Denton (2006), The differences between CME-driven storms and CIR-driven storms, *J. Geophys. Res.*, *111*, A07S08, doi:10.1029/2005JA011447.
Borovsky, J. E., and M. H. Denton (2009), Electron loss rates from the outer electron radiation belt caused by the filling of the outer plasmasphere: The calm before the storm, *J. Geophys. Res.*, *114*, A11203, doi:10.1029/2009JA014063.
Borovsky, J. E., and M. H. Denton (2010a), Solar-wind turbulence and shear: A superposed-epoch analysis of corotating interaction regions at 1 AU, *J. Geophys. Res.*, *115*, A10101, doi:10.1029/2009JA014966.
Borovsky, J. E., and M. H. Denton (2010b), On the heating of the outer radiation belt to produce high fluxes of relativistic electrons: Measured heating rates for high-speed-stream-driven storms, *J. Geophys. Res.*, *115*, A12206, doi:10.1029/2010JA015342.
Borovsky, J. E., and M. H. Denton (2010c), The magnetic field at geosynchronous orbit during high-speed-stream-driven storms: Connections to the solar wind, the plasma sheet, and the outer electron radiation belt, *J. Geophys. Res.*, *115*, A08217, doi:10.1029/2009JA015116.
Borovsky, J. E., and M. H. Denton (2013), The differences between storms driven by helmet-streamer CIRs and storms driven by pseudostreamer CIRs, *J. Geophys. Res. Space Physics*, *118*, 5506–5521, doi:10.1002/jgra.50524.
Borovsky, J. E., and M. H. Denton (2014), Exploring the cross-correlations and autocorrelations of the ULF indices and incorporating the ULF indices into the systems science of the solar-wind-driven magnetosphere, *J. Geophys. Res. Space Physics*, *119*, 4307–4334, doi:10.1002/2014JA019876.
Borovsky, J. E., and S. P. Gary (2014), How important are the alpha-proton relative drift and the electron heat flux for the proton heating of the solar wind in the inner heliosphere?, *J. Geophys. Res. Space Physics, 119*, 5210–5219, doi:10.1002/2014JA019758.
Borovsky, J. E., and J. T. Steinberg (2006), The freestream turbulence effect in solar-wind/magnetosphere coupling: Analysis through the solar cycle and for various types of solar wind, in *Recurrent Magnetic Storms: Corotating Solar Wind Streams*, 59 pp., AGU, Washington, D. C.
Borrini, G., J. T. Gosling, S. J. Bame, W. C. Feldman, and J. M. Wilcox (1981), Solar wind helium and hydrogen structure near the heliospheric current sheet: A signal of coronal streamers at 1 AU, *J. Geophys. Res.*, *86*, 4565–4573.
Bothmer, V., and R. Schwenn (1996), Signatures of fast CMEs in interplanetary space, *Adv. Space Res.*, *17*(4/5), 319.
Bruno, R., and V. Carbone (2013), The solar wind as a turbulence laboratory, *Living Rev. Solar Phys.*, *102*. [Available at http://www.livingreview.org/lrsp-2013-2.]
Burke, W. J. (2011), Solar cycle dependence of solar wind energy coupling to the thermosphere, *J. Geophys. Res.*, *116*, A06302, doi:10.1029/2011JA016437.
Burlaga, L., E. Sittler, F. Mariani, and R. Schwenn (1981), Magnetic loop behind an interplanetary shock: Voyager, Helios, and IMP 8 observations, *J. Geophys. Res.*, *80*, 6673–6684.
Cane, H. V., and I. G. Richardson (2003), Interplanetary coronal mass ejections in the near-Earth solar wind during 1996–2002, *J. Geophys. Res.*, *108*, 1156, doi:10.1029/2002JA009817.
Cranmer, S. R. (2009), Coronal holes, *Living Rev. Solar Phys.*, *6*, 3.
Crooker, N. U., G. L. Siscoe, S. Shodhan, D. F. Webb, J. T. Gosling, and E. J. Smith (1993), Multiple heliospheric current sheets and coronal streamer belt dynamics, *J. Geophys. Res.*, *98*, 9371–9381.
Crooker, N. U., S. W. Kahler, D. E. Larson, and R. P. Lin (2004a), Large-scale magnetic field inversions at sector boundaries, *J. Geophys. Res.*, *109*, A03108, doi:10.1029/2003JA010278.
Crooker, N. U., C.-L. Huang, S. M. Lamassa, D. E. Larson, S. W. Kahler, and H. E. Spence (2004b), Heliospheric plasma sheets, *J. Geophys. Res.*, *109*, A03107, doi:10.1029/2003JA010170.
Crooker, N. U., S. K. Antiochos, X. Zhao, and M. Neugebauer (2012), Global network of slow solar wind, *J. Geophys. Res.*, *117*, A04104, doi:10.1029/2011JA017236.
D'Amicis, R., R. Bruno, and B. Bavassano (2011), Response of the geomagnetic activity to solar wind turbulence during solar cycle 23, *J. Atmos. Sol. Terr. Phys.*, *73*, 653.
Echer, E., W. D. Gonzalez, B. T. Tsurutani, and A. L. C. Gonzalez (2008), Interplanetary conditions causing intense geomagnetic storms ($Dst <= -100$ nT) during solar cycle 23 (1996–2006), *J. Geophys. Res.*, *113*, A05221, doi:10.1029/2007JA012744.
Elliott, H. A., D. J. McComas, N. A. Schwadron, J. T. Gosling, R. M. Skoug, G. Gloeckler, and T. H. Zurbuchen (2005), An improved expected temperature formula for identifying ICMEs, *J. Geophys. Res.*, *110*, A04103, doi:10.1029/2004JA010794.
Elliott, H. A., C. J. Henney, D. J. McComas, C. W. Smith, and B. J. Vasquez (2012), Temporal and radial variation of the solar wind temperature-speed relationship, *J. Geophys. Res.*, *117*, A09102, doi:10.1029/2011JA017125.
Eyni, M., and R. Steinitz (1978), Cooling of slow solar wind protons from the Helios 1 experiment, *J. Geophys. Res.*, *83*, 4387–4388.
Feldman, U., E. Landi, and N. A. Schwadron (2005), On the sources of fast and slow solar wind, *J. Geophys. Res.*, *110*, A07109, doi:10.1029/2004JA010918.
Fisk, L. A., T. H. Zurbuchen, and N. A. Schwadron (1999), Coronal magnetic field: Consequences of large-scale motion, *Astrophys. J.*, *521*, 868.
Foullon, C., et al. (2011), Plasmoid releases in the heliospheric current sheet and associated coronal hole boundary layer evolution, *Astrophys. J.*, *737*, 1.
Foullon, C. B., et al. (2009), The apparent layered structure of the heliospheric current sheet: Multi-spacecraft observations, *Sol. Phys.*, *259*, 389.
Freeman, J. W., and R. E. Lopez (1985), The cold solar wind, *J. Geophys. Res.*, *90*, 9885–1997.
Georgieva, K., B. Kirov, and E. Gavruseva (2006), Geoeffectiveness of different solar drivers, and long-term variations of the correlation between sunspot and geomagnetic activity, *Phys. Chem. Earth*, *21*, 81.

Georgieva, K., B. Kirov, P. Koucka Knizova, Z. Mosna, B. Kouba, and Y. Asenovska (2012), Solar influences on atmospheric circulation, *J. Atmos. Sol. Terr. Phys.*, *90–91*, 15.
Georgieva, K., B. Kirov, and Y. A. Nagovitsyn (2013), Long-term variations of solar magnetic fields derived from geomagnetic data, *Geom. Aeron.*, *53*, 852.
Gloeckler, G., et al. (1998), Investigation of the composition of solar and interstellar matter using solar wind and pickup ion measurements with SWICS and SWIMS on the ACE spacecraft, *Space Sci. Rev.*, *86*, 497.
Gopalswamy, N. (2006), Coronal mass ejections of Solar Cycle 23, *J. Astrophys. Astr.*, *27*, 243.
Gosling, J. T. (1993), The solar flare myth, *J. Geophys. Res.*, *98*, 18,937–18,949.
Gosling, J. T., and R. M. Skoug (2002), On the origin of radial magnetic fields in the heliosphere, *J. Geophys. Res.*, *107*(A10), 1327, doi:10.1029/2002JA009734.
Gosling, J. T., V. Pizzo, and S. J. Bame (1973), Anomalously low proton temperatures in the solar wind following interplanetary shock waves—Evidence for magnetic bottles, *J. Geophys. Res.*, *78*, 2001–2009.
Gosling, J. T., G. Borrini, J. R. Asbridge, S. J. Bame, W. C. Feldman, and R. T. Hansen (1981), Coronal streamers in the solar wind at 1 AU, *J. Geophys. Res.*, *86*, 5438–5448.
Gosling, J. T., D. N. Baker, S. J. Bame, W. C. Feldman, R. D. Zwickl, and E. J. Smith (1987), Bidirectional solar wind electron heat flux events, *J. Geophys. Res.*, *92*, 8519–8535.
Habbal, S. R., H. Morgan, J. Johnson, M. B. Arndt, A. Daw, S. Jaeggli, J. Kuhn, and D. Mickey (2007), Localized enhancements of Fe^{+10} density in the corona as observed in Fe XI 789.2 nm during the 2006 March 29 total solar eclipse, *Astrophys. J.*, *663*, 598.
Hellinger, P., L. Matteini, S. Stverak, P. M. Travnicek, and E. Marsch (2011), Heating and cooling of protons in the fast solar wind between 0.3 and 1 AU: Helios revisited, *J. Geophys. Res.*, *116*, A09105, doi:10.1029/2011JA016674.
Hirshberg, J., J. R. Asbridge, and D. E. Robbins (1974), The helium component of solar wind velocity streams, *J. Geophys. Res.*, *79*, 934–938.
Intriligator, D. S. (1974), Evidence of solar-cycle variations in the solar wind, *Astrophys. J.*, *188*, L23.
Jian, L., C. T. Russell, J. G. Luhmann, and R. M. Skoug (2006), Properties of interplanetary coronal mass ejections at one AU during 1995–2004, *Sol. Phys.*, *239*, 393.
Kasper, J. C., M. L. Stevens, K. E. Korreck, B. A. Maruca, K. K. Kieffer, N. A. Scwadron, and S. T. Lepri (2012), Evolution of the relationships between helium abundance, minor ion charge state, and solar wind speed over the solar cycle, *Astrophys. J.*, *745*, 162.
King, J. H., and N. E. Papitashvili (2005), Solar wind spatial scales in and comparisons of hourly Wind and ACE plasma and magnetic field data, *J. Geophys. Res.*, *110*, A02104, doi:10.1029/2004JA010649.
Klein, L. W., and L. F. Burlaga (1982), Interplanetary magnetic clouds at 1 AU, *J. Geophys. Res.*, *87*, 613–624.
Landi, E., R. L. Alexander, J. R. Gruesbeck, J. A. Gilbert, S. T. Lepri, W. B. Manchester, and T. H. Zurbuchen (2012), Carbon ionization stages as a diagnostic of the solar wind, *Astrophys. J.*, *744*, 100.
Lavraud, B., and J. E. Borovsky (2008), Altered solar wind-magnetosphere interaction at low Mach numbers: Coronal mass ejections, *J. Geophys. Res.*, *113*, A00B08, doi:10.1029/2008JA013192.
Lepping, R. P., C.-C. Wu, and D. B. Berdichevsky (2005), Automatic identification of magnetic cloud-like regions at 1 AU: Occurrence rate and other properties, *Ann. Geophys.*, *23*, 2687.
Lepri, S. T., E. Landi, and T. H. Zurbuchen (2013), Solar wind heavy ions over solar cycle 23: ACE/SWICS measurements, *Astrophys. J.*, *768*, 94.
Liu, Y. D., et al. (2014), Observations of an extreme storm in interplanetary space caused by successive coronal mass ejections, *Nature Comm.*, doi:10.1038/ncomms4481.
Lopez, R. E. (1987), Solar cycle invariance in solar wind proton temperature relationships, *J. Geophys. Res.*, *92*, 11,189.
Lopez, R. E., J. W. Freeman, and E. C. Roelof (1986), The relationship between proton temperature and momentum flux density in the solar wind, *Geophys. Res. Lett.*, *13*, 640–643.
Lopez, R. E., V. G. Merkin, and J. G. Lyon (2011), The role of the bow shock in solar wind-magnetosphere coupling, *Ann. Geophys.*, *29*, 1129.
Luttrell, A. H., and A. K. Richter (1988), The role of Alfvénic fluctuations in MHD turbulence evolution between 0.3 and 1 AU, in *Proceedings of the Sixth International Solar Wind Conference*, *NCAR TN-306*, edited by V. J. Pizzo, T. E. Holzer, and D. G. Sime, 335 pp., Boulder, Colo.
Mariani, F., B. Bavassano, and U. Villante (1983), A statistical study of MHD discontinuities in the inner solar system: Helios 1 and 2, *Sol. Phys.*, *83*, 349.
Marsch, E., K.-H. Muhlhauser, H. Rosenbauer, R. Schwenn, and F. M. Neubauear (1982), Solar wind helium ions: Observations of the Helios solar probes between 0.3 and 1 AU, *J. Geophys. Res.*, *87*, 35–51.
Masters, A., et al. (2013), In situ observations of high-Mach number collisionless shocks in space plasmas, *Plasma Phys. Control. Fusion*, *55*, 124,035.
Matsumoto, Y., T. Amano, and M. Hoshino (2013), Electron acceleration in a nonrelativistic shock with very high Alfvén Mach number, *Phys. Rev. Lett.*, *111*, 215,003.
Matthaeus, W. H., B. Breech, P. Dmitruk, A. Bemporad, G. Poletto, M. Velli, and M. Romoli (2007), Density and magnetic field signatures of interplanetary 1/f noise, *Astrophys. J.*, *657*, L121.
McComas, D. J., S. J. Blame, P. Barker, W. C. Feldman, J. L. Phillips, P. Riley, and J. W. Griffee (1998), Solar Wind Electron Proton Alpha Monitor (SWEPAM) for the advanced composition explorer, *Space Sci. Rev.*, *86*, 563.
McIntosh, S. W., K. K. Diefer, R. J. Leamon, J. C. Kasper, and M. L. Stevens (2011), Solar cycle variations in the elemental abundance of helium and fractionation of iron in the fast solar wind: Indicators of an evolving energetic release of mass from the lower solar atmosphere, *Astrophys. J. Lett.*, *740*, L23.
McPherron, R. L., L. Kepko, T. I. Pulkkinen, T. S. Hsu, J. W. Weygand, and L. F. Bargatze (2009), Changes in the response of the *AL* index with solar cycle and epoch within a corotating interaction region, *Ann. Geophys.*, *27*, 3165.
McPherron, R. L., D. N. Baker, T. I. Pulkkinen, T.-S. Hsu, J. Kissinger, and X. Chu (2013), Changes in solar wind-magnetosphere coupling with solar cycle, season, and time relative to stream interfaces, *J. Atmos. Sol. Terr. Phys.*, *99*, 1.
Murphy, N., E. J. Smith, and N. A. Schwadron (2002), Strongly underwound magnetic fields in co-rotating rarefaction regions: Observations and implications, *Geophys. Res. Lett.*, *29*(22), 2066, doi:10.1029/2002GL015164.
Nagatsuma, T. (2006), Diurnal, semiannual, and solar cycle variations of solar wind-magnetosphere-ionosphere coupling, *J. Geophys. Res.*, *111*, A09202, doi:10.1029/2005JA011122.
Nakai, H., and Y. Kamide (1999), Solar cycle variations in the storm-substorm relationship, *J. Geophys. Res.*, *104*, 22,695–22,700.
Neugebauer, M., and R. Goldstein (1997), Particle and field signatures of coronal mass ejections in the solar wind, *Geophys. Monogr.*, *99*, 245.
Neugebauer, M., R. Goldstein, and B. E. Goldstein (1997), Features observed in the trailing regions of interplanetary clouds from coronal mass ejections, *J. Geophys. Res.*, *102*, 19,743–19,751.

Neugebauer, M., J. T. Steinberg, R. L. Tokar, B. L. Barraclough, E. E. Dors, R. C. Weins, D. E. Gingerich, D. Luckey, and D. B. Whiteaker (2003), Genesis on-board determination of the solar wind flow regime, *Space Sci. Rev.*, *105*, 661.
Neugebauer, M., P. C. Liewer, B. E. Goldstein, X. Zhou, and J. T. Steinberg (2004), Solar wind stream interaction regions without sector boundaries, *J. Geophys. Res.*, *109*, A10102, doi:10.1029/2004JA010456.
Onsager, T. G., J. C. Green, G. D. Reeves, and H. J. Singer (2007), Solar wind and magnetospheric conditions leading to the abrupt loss of outer radiation belt electrons, *J. Geophys. Res.*, *112*, A01202, doi:10.1029/2006JA011708.
Orlove, S. T., C. W. Smith, B. J. Vasquez, N. A. Schwadron, R. M. Skoug, T. H. Zurbuchen, and L. Zhao (2013), Intervals of radial interplanetary magnetic fields at 1 AU, their association with rarefaction regions, and their apparent magnetic foot points at the Sun, *Astrophys. J.*, *774*, 15.
Owens, M. J., C. N. Arge, H. E. Spence, A. Pembroke (2005), An event-based approach to validating solar wind speed predictions: High speed enhancements in the Wang-Sheeley-Arge model, *J. Geophys. Res.*, *110*, A12105, doi:10.1029/2005JA011343.
Pagel, A. C., N. U. Crooker, T. H. Zurbuchen, and J. T. Gosling (2004), Correlation of solar wind entropy and oxygen ion charge state ratio, *J. Geophys. Res.*, *109*, A01113, doi:10.1029/2003JA010010.
Panasenco, O., and M. Velli (2013), Coronal pseudostreamers: Source of fast or slow solar wind?, *AIP Conf. Proc.*, *1539*, 50.
Parenti, S., B. J. I. Bromage, G. Poletto, G. Noci, J. C. Raymond, and G. E. Bromage (2000), Characteristics of solar coronal streamers, *Astron. Astrophys.*, *363*, 800.
Pneuman, G. W. (1968), Some general properties of helmeted coronal structures, *Sol. Phys.*, *3*, 578.
Poomvises, W., J. Zhang, and O. Olmedo (2010), Coronal mass ejection propagation and expansion in three-dimensional space in the heliosphere based on STEREO/SECCHI observations, *Astrophys. J. Lett.*, *717*, L159.
Raymond, J. C., et al. (1997), Composition of coronal streamers from the SOHO Ultraviolet Coronagraph Spectrometer, *Solar Phys.*, *175*, 645.
Reisenfeld, D. B., J. T. Steinberg, B. L. Barraclough, E. E. Dors, R. C. Weins, M. Neugebauer, A. Reinard, and T. Zurbuchen (2003), Comparison of the Genesis solar wind regime algorithm results with solar wind composition observed by ACE, *Am. Phys. Soc. Conf. Proc.*, *679*, 632.
Richardson, I. G. (2013), What in the solar wind does the Earth react to?, *AIP Conf. Proc.*, *1539*, 370.
Richardson, I. G., and H. V. Cane (1995), Regions of abnormally low proton temperature in the solar wind (1965–1991) and their association with ejecta, *J. Geophys. Res.*, *100*, 23,397.
Richardson, I. G., and H. V. Cane (1996), Particle flows observed in ejecta during solar event onsets and their implication for the magnetic field topology, *J. Geophys. Res.*, *101*, 27,521.
Richardson, I. G., and H. V. Cane (2004), The fraction of interplanetary coronal mass ejections that are magnetic clouds: Evidence for a solar cycle variation, *Geophys. Res. Lett.*, *31*, L18804, doi:10.1029/2004GL020958.
Richardson, I. G., and H. V. Cane (2010), Near-Earth interplanetary coronal mass ejections during solar cycle 23 (1996–2009): Catalog and summary of properties, *Sol. Phys.*, *264*, 189.
Richardson, I. G., and H. V. Cane (2012), Near-Earth solar wind flows and related geomagnetic activity during more than four solar cycles (1963–2011), *J. Space Weather Space Clim.*, *2*, A02.
Richardson, I. G., E. W. Cliver, and H. V. Cane (2000), Sources of geomagnetic activity over the solar cycle: Relative importance of coronal mass ejections, high-speed streams, and slow solar wind, *J. Geophys. Res.*, *105*, 18,203.
Richardson, I. G., E. W. Cliver, and H. V. Cane (2001), Sources of geomagnetic storms for solar minimum and maximum conditions during 1972–2000, *Geophys. Res. Lett.*, *28*, 2569.
Riley, P., and J. G. Luhmann (2012), Interplanetary signatures of unipolar streamers and the origin of the slow solar wind, *Sol. Phys.*, *277*, 355.
Riley, P., and J. T. Gosling (2007), On the origin of near-radial magnetic fields in the heliosphere: Numerical simulations, *J. Geophys. Res.*, *112*, A06115, doi:10.1029/2006JA012210.
Rostoker, G., and C.-G. Falthammar (1967), Relationship between changes in the interplanetary magnetic field and variations in the magnetic field at the Earth's surface, *J. Geophys. Res.*, *72*, 5853.
Rusin, V., M. Druckmuller, P. Aniol, M. Minarovjech, M. Saniga, Z. Mikic, J. A. Linker, R. Lionello, P. Riley, and V. S. Titov (2010), Comparing eclipse observations of the 2008 August 1 solar coronal with an MHD model prediction, *Astron. Astrophys.*, *513*, A45.
Schwadron, N. A., C. W. Smith, H. E. Spence, J. C. Kasper, K. Korreck, M. L. Stevens, B. A. Baruca, K. K. Kiefer, S. T. Lepri, and D. McComas (2011), Coronal electron temperature from the solar wind scaling law throughout the space age, *Astrophys. J.*, *739*, 9.
Schwenn, R. (1990), Large scale structure of the interplanetary medium, in *Physics of the Inner Heliosphere I*, edited by R. Schwenn and E. Marsch, 99 pp., Springer, Berlin.
Schwenn, R. (2006), Solar wind sources and their variations over the solar cycle, *Space Sci. Rev.*, *124*, 51.
Sheeley, N. R., Jr., J. W. Harvey, and W. C. Feldman (1976), Coronal holes, solar wind streams, and recurrent geomagnetic disturbances: 1973–1976, *Solar Phys.*, 49–271.
Skoug, R. M., W. C. Feldman, J. T. Gosling, D. J. McComas, and C. W. Smith (2000), Solar wind electron characteristics inside and outside coronal mass ejections, *J. Geophys. Res.*, *105*, 23,069–23,084.
Skoug, R. M., J. T. Gosling, J. T. Steinberg, D. J. McComas, C. W. Smith, N. F. Ness, Q. Hu, and L. F. Burlaga (2004), Extremely high speed solar wind: 29–30 October 2003, *J. Geophys. Res.*, *109*, A09102, doi:10.1029/2004JA010494.
Smith, C. W., and J. L. Phillips (1996), The role of CMEs and interplanetary shocks in IMF winding angle statistics, *AIP Conf. Proc.*, *382*, 502.
Smith, C. W., M. H. Acuna, L. F. Burlaga, J. L'Heureux, N. F. Ness, and J. Scheifele (1998), The ACE magnetic fields experiment, *Space Sci. Rev.*, *86*, 611.
Snyder, C., M. Neugebauer, and U. R. Rao (1963), The solar wind velocity and its correlation with cosmic-ray variations and with solar and geomagnetic activity, *J. Geophys. Res.*, *68*, 6361–6370.
Steinberg, J. T., J. T. Gosling, R. M. Skoug, and R. C. Wiens (2005), Suprathermal electrons in high-speed streams from coronal holes: Counterstreaming on open field lines at 1 AU, *J. Geophys. Res.*, *110*, A06103, doi:10.1029/2005JA011027.
Subramanian, S., M. S. Madjarska, and J. G. Doyle (2010), Coronal hole boundaries evolution at small scales II. XRT view. Can small-scale outflows at CHBs be a source of the slow solar wind?, *Astron. Astrophys.*, 516, A50.
Suess, S. T., Y.-K. Ko, R. Von Steiger, and R. L. Moore (2009), Quiescent current sheets in the solar wind and origins of slow wind, *J. Geophys. Res.*, *114*, A04103, doi:10.1029/2008JA013704.
Susino, R., R. Ventura, D. Spadaro, A. Vourlidas, and E. Landi (2008), Physical parameters along the boundaries of a mid-latitude streamer and its adjacent regions, *Astron. Astrophys.*, *488*, 303.
Thieme, K. M., E. Marsch, and R. Schwenn (1988), Relationship between structures in the solar wind and their source regions in the corona, in *Proceedings of the Sixth International Solar Wind Conference*, vol. 1, edited by V. J. Pizzo, T. Holzer, and D. G. Sime, 317 pp., *Tech. Note NCAR/TN-306+Proc*, Natl. Cent. for Atmos. Res., Boulder, Colo.
Thieme, K. M., R. Schwenn, and E. Marsch (1989), Are structures in high-speed streams signatures of coronal fine structures?, *Adv. Space Res.*, *9*(4), 127.

Thieme, K. M., E. Marsch, and R. Schwenn (1990), Spatial structures in high-speed streams as signatures of fine structures in coronal holes, *Ann. Geophys.*, *8*, 713.

Thomsen, M. F. (2004), Why *Kp* is such a good measure of magnetospheric convection, *Space Weather*, *2*, S11044, doi:10.1029/2004SW000089.

Tu, C.-Y., and E. Marsch (1995), MHD structures, waves and turbulence in the solar wind, *Space Sci. Rev.*, *73*, 1.

von Steiger, R., T. H. Zurbuchen, and D. J. McComas (2010), Oxygen flux in the solar wind: Ulysses observations, *Geophys. Res. Lett.*, *37*, L22101, doi:10.1029/2010GL045389.

Wang, Y.-M., and N. R. Sheeley Jr. (1990), Solar wind speed and coronal flux-tube expansion, *Astrophys. J.*, *355*, 726.

Wang, Y.-M., N. R. Sheeley Jr., D. G. Socker, R. A. Howard, and N. B. Rich (2000), The dynamical nature of coronal streamers, *J. Geophys. Res.*, *105*, 25,113–25,142.

Wang, Y.-M., J. B. Biersteker, N. R. Sheeley Jr., S. Koutchmy, J. Mouette, and M. Druckmuller (2007), The solar eclipse of 2006 and the origin of raylike features in the white-light corona, *Astrophys. J.*, *660*, 882.

Wang, Y.-M., R. Grappin, E. Robbecht, and N. R. Sheeley Jr. (2012), On the nature of the solar wind from coronal pseudostreamers, *Astrophys. J.*, *749*, 182.

Wing, S., and D. G. Sibeck (1997), Effects of interplanetary magnetic field *z* component and the solar wind dynamic pressure on the geosynchronous magnetic field, *J. Geophys. Res.*, *102*, 7207–7216.

Winterhalter, D., E. J. Smith, M. E. Burton, N. Murphy, and D. J. McComas (1994), The heliospheric plasma sheet, *J. Geophys. Res.*, *99*, 6667–6680.

Wurz, P., M. R. Aellig, F. M. Ipavich, S. Hefti, P. Bochsler, A. B. Galvin, H. Grunwaldt, M. Hilchenback, F. Gliem, and D. Hovestadt (1999), The iron, silicon and oxygen abundance in the solar wind measured with SOHO/CELIAS/MTOF, *Phys. Chem. Earth (C)*, *24*, 421.

Xystouris, G., E. Sigala, and H. Mavromichalaki (2014), A complete catalog of high-speed solar wind streams during solar cycle 23, *Sol. Phys.*, *289*, 995.

Yordanova, E., A. Balogh, A. Noullez, and R. von Steiger (2009), Turbulence and intermittency in the heliospheric magnetic field in fast and slow solar wind, *J. Geophys. Res. 114*, A08101, doi:10.1029/2009JA014067.

Zastenker, G. N., I. V. Koloskova, M. O. Riazantseva, A. S. Yurasov, J. Safrankova, Z. Nemecek, L. Prech, and P. Cagas (2014), Observation of fast variations of the helium-ion abundance in the solar wind, *Cosmic Res.*, *52*, 25.

Zhang, J., et al. (2007), Solar and interplanetary sources of major geomagnetic storms ($Dst <= -100$ nT) during 1996–2005, *J. Geophys. Res.*, *112*, A10102, doi:10.1029/2007JA012321.

Zhang, X.-Y., M. B. Moldwin, J. T. Steinberg, and R. M. Skoug (2014), Alfvén waves as a possible source of long-duration, large-amplitude, and geoeffective southward IMF, *J. Geophys. Res. Space Physics*, *119*, 3259–3266, doi:10.1002/2013JA019623.

Zhao, L., T. H. Zurbuchen, and L. A. Fisk (2009), Global distribution of the solar wind during solar cycle 23: ACE observations, *Geophys. Res. Lett.*, *36*, L14104, doi:10.1029/2009GL039181.

Zurbuchen, T. H., and I. G. Richardson (2006), In-situ solar wind and magnetic field signatures of interplanetary coronal mass ejections, *Space Sci. Rev.*, *123*, 31.

Zurbuchen, T. H., L. A. Fisk, G. Gloeckler, and R. von Steiger (2002), The solar wind composition throughout the solar cycle: A continuum of dynamic states, *Geophys. Res. Lett.*, *29*(9), 1352, doi:10.1029/2001GL013946.